



School of Chemistry

The use of Spectroscopic methods to determine
the state of Plasmas relevant to the Chemical
Vapour Deposition of Diamond

John Allden

15th April 2019

This thesis is submitted in partial fulfilment of the requirements
for the Honours Degree of MSci at the University of Bristol

Supervisor: Professor M. N. R Ashfold

Second Assessor: Professor P. W. May

Third Assessor: Professor C. M. Western

Section: Physical and Theoretical

Abstract

This thesis investigates several microwave activated H based plasmas, employing two established plasma diagnostic techniques; Optical Emission Spectroscopy (OES) and Cavity Ring Down Spectroscopy (CRDS) to probe the gas phase and surface chemistry.

The first use of OES was carried out on $H_2(d-a)$ and H_α emissions to demonstrate the notable effects that Ar, substrate diameter, and substrate-baseplate spacer wire thickness have on the gas phase chemistry, inferred from the observed changes in these emissions. The control these parameters impart on the substrate temperature was of particular interest. Previous studies have demonstrated that these emission intensities are sensitive to the hyperthermal component of the electron energy distribution function (EEDF), and this was reaffirmed in this study. Increasing the input mole fraction of Ar, decreasing the substrate diameter and increasing wire thickness was found to enhance the substrate temperature, and in the case of latter two variations, the absolute intensities of $H_2(d-a)$ and H_α emissions at low plasma heights. The interpretation is that these two parameters enhance the hyperthermal component of the EEDF at these low heights. Introducing Ar, comparatively, reduced these emissions, but enhanced their relative intensities at the low plasma heights. Previous studies have attributed this to near resonant energy transfers between excited states of Ar, H and H_2 .

The nature of these emissions does not allow sampling of the thermal component of the EEDF. Al was shown to have range of energy levels suitable for sampling this component of the EEDF, and was introduced into the gas phase by etching of Al and Al_2O_3 substrates. A number of emissions originating from Al and H were investigated as a function of total pressure, microwave power, spacer wire thickness and Ar flow rate with an Al_2O_3 substrate present. Al emissions were localised to low plasma heights, highlighting a flaw with the chosen method of introduction. Nonetheless, Al demonstrated enhanced emission intensities with increasing pressure and microwave power, attributed to an increase in substrate temperature, and decreased emissions with Ar addition, suggesting Ar may act to quench the investigated excited states of Al. H_β emissions were also monitored as a function of these conditions, and demonstrated notably different trends to the H_α measured previously. This indicates a significant change to the hyperthermal component of the EEDF when Al is present. As a probe of the thermal component of the EEDF, it was the intention that Al would provide an estimate of electron temperature from the ratio of its emission line intensities. At first assessment, Al did not offer a solution to the challenge of effectively measuring the electron temperature of microwave activated plasmas.

The final component of this thesis aimed to contribute towards a working interpretation of microwave activated H/Si and H/C/Si gas phase chemistry, beneficial to the development of Si doped diamond. Column density measurements of Si were carried out using CRDS as a function of pressure, microwave power and SiH_4 input gas fraction, both with and without the presence of CH_4 . These experiments were carried out on three absorption transitions of Si atoms. It was deduced that Si content maximises in the cooler regions of the plasma, and that the behaviour of Si with varying SiH_4 fraction and the measured column densities were sensitive to changes in the experimental gas exchange. Generally Si content increased with increasing Si mole fraction and pressure, in other words the total number density of Si, whether this was achieved by varying SiH_4 fraction or pressure itself. Many of these results were reproduced in the presence of CH_4 . Upon the introduction of CH_4 , it is deduced that Si atoms react preferentially with CH_x ($0 \leq x \leq 4$) species when compared to C_2H_2 .

Acknowledgments

First and foremost, I would like to thank Edward Mahoney for his unwavering support and patience, without whom I would not have got past the title page. Secondly, I could not have asked for a friendlier supervisor in Professor Mike Ashfold, whose assistance was invaluable and always available, and thoughtfulness greatly appreciated.

I offer my wholehearted gratitude to Professor Paul May and the extended Diamond Group for their approachability and first-rate conversation; notably Amelia Billings and Heather Bolton as my fellow MSci students, for their enthusiasm and laughter.

Lastly, I thank my family and friends for getting me this far.

Contents

Abbreviations	4
1. Introduction	6
1.1 The Diamond Standard.....	6
1.1.1 <i>Diamond</i>	6
1.1.2 <i>Graphite</i>	7
1.2 High-Pressure High-Temperature	7
1.3 Chemical Vapour Deposition	8
1.3.1 <i>Gas Phase Chemistry</i>	10
1.4 Dopants and Additional Species	13
1.4.1 <i>Silicon</i>	14
1.4.2 <i>Argon</i>	15
1.5 Spectroscopic Methods	15
1.5.1 <i>Optical Emission Spectroscopy</i>	15
1.5.2 <i>Cavity Ring Down Spectroscopy</i>	16
1.6 Aims	17
1.7 References	18
2. Experimental	20
2.1 Microwave Plasma Chemical Vapour Deposition	20
2.1.1 <i>Reactor</i>	20
2.1.2 <i>Substrate Variables</i>	21
2.1.3 <i>Addition of Argon, Silane and Methane</i>	22
2.2 Spectroscopy.....	22
2.2.1 <i>Optical Emission Spectroscopy</i>	22
2.2.2 <i>Cavity Ring Down Spectroscopy</i>	23
2.3 References	26
3. Results and Discussion	27
3.1 Optical Emission Spectroscopy of Hydrogen Plasmas.....	27
3.2 Substrate Temperature Control	28
3.2.1 <i>H₂(d-a) and H_α as a function of Argon Flow Rate</i>	28
3.2.1 <i>H₂(d-a) and H_α as a function of Substrate Diameter</i>	29
3.2.1 <i>H₂(d-a) and H_α as a function of Wire Spacer Diameter</i>	30
3.3 Probing Electron Temperature through Aluminium Emissions	32
3.3.1 <i>Aluminium Substrate</i>	32
3.3.2 <i>Aluminium Oxide Substrate</i>	33
3.4 Cavity Ring Down Spectroscopy of Silicon Atoms	40
3.4.1 <i>H/Si Plasma</i>	41
3.4.2 <i>H/C/Si Plasma</i>	43
3.5 References	44
4. Conclusions and Further Work	45
4.1 Substrate Temperature Control	45
4.2 Probing Electron Energy Distribution Functions through Aluminium Emissions.....	45
4.3 Cavity Ring Down Spectroscopy of Silicon Atoms	47
4.4 References	48

Abbreviations

C - Carbon

CVD – Chemical Vapour Deposition

HPHT – High-Pressure High-Temperature

λ – Wavelength

2D – Two Dimensional

ASEA – Allmänna Svenska Elektriska Aktiebolaget

CO – Carbon monoxide

H₂ – Hydrogen gas/molecular hydrogen

H – Atomic hydrogen

HF – Hot-Filament

NIRIM – National Institute for Research in Inorganic Materials

MWPCVD – Microwave Plasma Chemical Vapour Deposition

T_{gas} – Local gas temperature / K or °C

ASTEX – Applied Science and Technology Inc.

PCD – Poly-Crystalline diamond

SCD – Single Crystal Diamond

T_{sub} – Substrate temperature / K or °C

[X] – Number density of species X

d_{wire} – Substrate wire spacer diameter / "

C_xH_y – Carbon species

EI – Electron Impact

TD – Thermal Dissociation

p – Pressure / Torr

EIE – Electron Impact Excitation

H₃⁺ – Trihydrogen cation

X* - Excited species X

n_e – Electron density

$|E|$ - Electric Field

N – Number of gas particles

$|E|/N$ – Reduced electric field

EEDF – Electron Energy Distribution Function

F(X) – Flow rate of species, X / sccm

sccm – Standard cubic centimetres per minute

H/C plasma – Conventional CVD plasma

z – Height above the substrate / mm

r – Radius from the substrate centre / cm

B – Boron

N – Nitrogen

O – Oxygen

Si – Silicon

Ge – Germanium

X – Additional Species

B₂H₆ – Diborane

P – Phosphorus

N₂ – Nitrogen gas/molecular nitrogen

NV – Nitrogen Vacancy centre

SPS – Single Photon Source

ZPL – Zero-Phonon Line

SiV – Silicon Vacancy centre

SiH₄ – Silane

Ar – Argon

T_e – Electron temperature / eV

OES – Optical Emission Spectroscopy

CRDS – Cavity Ring Down Spectroscopy

REMPI – Resonance-Enhanced Multiphoton Ionization

MS – Mass Spectroscopy

MSBS – Molecular Beam Mass Spectroscopy

IR – Infrared

P – MW power / kW

d_{sub} – Substrate diameter / mm

DEA – Dissociative Electron Attachment

I_t – Detected Intensity

I_0 – Initial Intensity

t – Detection Time / s

τ – Ring-Down Lifetime / ns

A – Absorbance

Al – Aluminium

Al₂O₃ – Aluminium oxide

MFCs – Mass Flow Controllers

ppm – Parts per million

$X_0(X)$ – Molar fraction of species, X

ppt – parts per thousand

CCD – Charge Coupled Device

A_{ki} – Einstein A coefficient

λ_{obs} - Observed wavelength

NdYAG – Neodymium³⁺ doped yttrium aluminium garnet

J – Total angular momentum quantum number

g_i – Upper state degeneracy

g_k - Lower state degeneracy

λ_{absorb} - Absorption wavelength

MSE – Mean Squared Error

$\bar{\nu}$ – Wavenumber / cm⁻¹

τ_0 – Baseline ring-down lifetime / ns

L – Length between CRDS mirrors / cm

Al(1) – Al emission observed at 308.22 nm

Al(2) – Al emission observed at 309.27 nm

Al(3) – Al emission observed at 394.40 nm

Al(4) – Al emission observed at 396.15 nm

ε - Detection efficiency of the optical system at relevant λ

$k_Q[Q]$ - Rate of quenching of species, Q

k_{EIE} - Rate of EIE

$\eta(E)$ - η_e at the emission energy, E

ΔE – Energy difference between upper states

k_B - Boltzmann constant

{Si} – Column density of Si

1. Introduction

1.1 The Diamond Standard

1.1.1 Diamond

The concept of man-made diamond may still conjure imagery from the realms of alchemy, however 70 years of dedicated research has led to the synthesis of this carbon (C) allotrope becoming very real practice, with numerous applications. As of 2016, approximately 130 million carats of natural diamond were still being mined and processed yearly, whereas in the previous year over 120 million carats were produced through synthetic methods in the United States alone.^{1,2} The understanding of synthetic diamond and the methods by which it is prepared have expanded vastly since the conception of the Chemical Vapour Deposition (CVD) and High-Pressure High-Temperature (HPHT) methods in the 1950s, and by the turn of the millennia 9 out of 10 diamonds used for industrial purposes were synthetically sourced.³ The cause for this may lie in the exceptional standard of diamond as a material; its mechanical, optical and thermal properties are matched by no other material, and synthesising the structure responsible can be a rewarding undertaking. At present CVD is typically employed to grow thin-film diamond for use in optics and thermal management, while HPHT forms single crystals utilising its hardness for cutting and drilling tools.⁴

Diamond holds the accolades for lowest compressibility ($8.3 \times 10^{-13} \text{ m}^2 \text{ N}^{-1}$), highest room temperature thermal conductivity ($2100 \text{ W m}^{-1} \text{ K}^{-1}$) and highest sound propagation velocity ($1.75 \times 10^4 \text{ m s}^{-1}$) to name a few.^{4,5} It is often a combination of these superior properties that renders diamond highly appealing for many potential applications. Most familiarly diamond's supremacy as a gemstone relies upon both its mechanical and optical properties; the high refractive index and wavelength (λ) dispersion contributes to diamonds visual brilliance while its strength and stability adorn diamond with longevity and permanency.⁵ Diamond commonly exists as a covalent cubic lattice (figure 1.1a), naturally an octahedral unit cell with {100}, {110} and {111} planes. The sp^3 hybridised structure with tetrahedral σ coordination uses all four valence electrons and results in an incredibly strong bonding arrangement that surpasses all other materials on bulk modulus ($1.2 \times 10^{12} \text{ N m}^{-2}$) and atom density (3.525 g cm^{-3}).^{4,6,7} Diamond's structure is integral to its super-standard properties, that largely arise as a consequence of its directional coordination and subsequent isotropy. Any weakness tends to arise from structural defects, impurities and grain boundaries. Notably diamond cleavage is most easily achieved along the {111} plane.⁵

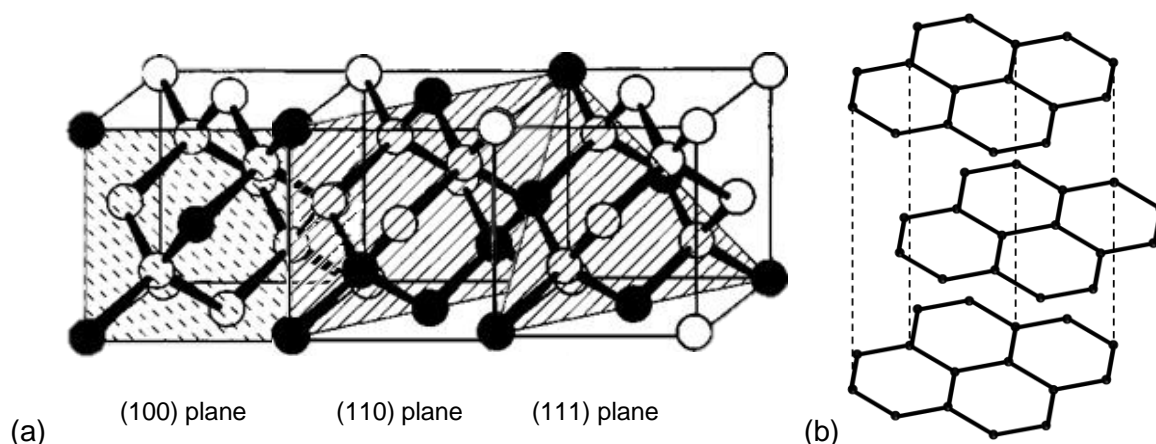


Figure 1.1: The structures of a) diamond and b) graphite.

1.1.2 Graphite

C forms numerous allotropes with a variety of structural features; through sp^2 hybridisation, C may exist as graphite (figure 1.1b). Graphite was seen as a starting point for diamond synthesis; trigonal σ bonded atoms form a planar network of hexagonal C rings.^{6,8} The fourth valence electron lies in the π orbital above and below the plane, capable of π - π interactions or delocalization.⁹ Predominantly however, weak Van der Waals interactions between the basal planes of graphite allow these layers to slide over one another resulting in its soft, lubricative macroscopic properties. Graphite possesses good thermal and chemical stability, alongside conductive properties offering copious applications, for instance the enhancement of polymer thermal conductivity.¹⁰ Graphite is mined from natural sources or made synthetically from amorphous forms of C, such as coke at temperatures nearing 3000 °C.⁸ In bulk form, graphite's physical properties are dependent on the isotropy of the crystals, but a number of its favourable qualities lie in the two-dimensional (2D) graphitic structure analogous to that of graphene.¹¹ Graphite is thermodynamically favoured over diamond, and consequentially a large energy barrier exists between the two allotropes. For this reason, initial efforts to synthesise diamond from graphite were conducted at high temperatures and pressures reflecting its natural formation.

1.2 High-Pressure High-Temperature

F. P. Bundy *et al.* working at General Electrical, were first to publish a HPHT method for synthesising diamond in 1955, however H. Liander *et al.* of Allmänna Svenska Elektriska Aktiebolaget (ASEA) in Sweden conceived a successful process in 1953.^{7,12} A simplified C phase diagram (figure 1.2) illustrates that at significant pressures, in the order of 20,000 atm, diamond becomes thermodynamically stable over graphite due to its denser nature, however in practice approximately 130,000 atm and 3300 K are required to drive the transformation.^{3,13} The production of diamond on thermodynamics alone is relatively impractical and chemical systems are typically employed to encourage its formation. Transition metals can act as solvent catalysts at conditions of 55,000 atm and 1600 K to reliably produce diamond, reducing the demand on pressure and temperature.³ C dissolves in the molten catalyst, affording mobility to the atoms and lowering the activation energy for conversion to diamond. Non-metallic catalysts also prove effective at more extreme conditions.¹⁴ Alternatively, pressurised graphite subjected to an explosion or direct heating at temperatures nearing 4000 K will form diamond due to this additional thermal energy permitting bond fission.³

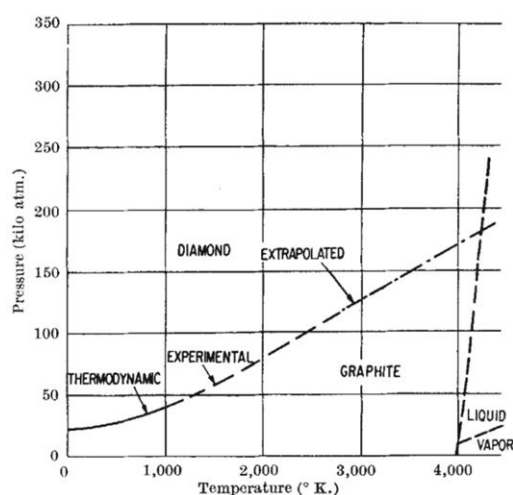


Figure 1.2: C phase diagram depicting the temperature pressure line between Graphite and Diamond.¹³

diamond due to this additional thermal energy permitting bond fission.³

The HPHT conditions require specialist reactors and a number of variations have been developed since its conception, notably the Hall Belt and toroid anvil.³ Both rely upon methods of compression over a small area to generate the large pressures required of diamond formation, and are typically made of tungsten carbide, a lattice comparable with that of diamond in order to withstand the compressive forces. Diamond growth by HPHT is limited by the volume of the reaction chamber and duration of synthesis, however it is not the sole method of diamond synthesis.

1.3 Chemical Vapour Deposition

In the same decade, a small number of researchers were investigating the growth of diamond at low pressures, with initial execution by W. G. Eversole of the Union Carbide Corporation in 1953; revealed in 1961 and 1962 in the form of patents.¹⁵ The deposition of diamond from an activated gas phase at low pressures has since become common practice in the formation of diamond films amongst other applications. CVD, unlike HPHT, does not overcome the thermodynamic barrier of diamond synthesis, but instead harnesses the kinetic favourability of diamond formation at gas temperatures of approximately 1400 K, close to a growing surface. At these conditions, the difference in thermodynamic stability between graphite and diamond is almost negligible, less than the value of kT , thus diamond may be deposited onto the surface from C-based gases.¹⁵

Eversole's success in the early 1950s came from the deposition of C onto diamond seeds from a heated gas phase consisting of CO (carbon monoxide).⁷ Aside from two former Soviet Union researchers; B. V. Spitsyn and B. V. Deryagin who achieved low-pressure diamond growth from C halides in 1956, there were few further considerable findings that decade.^{15,16} The 1960s marked an apparent resurgence in efforts to further develop low-pressure, metastable synthesis. In the United States (U.S.) in 1964 H. J. Hibshman, like Eversole used CO as his precursor gas, however he combined it with hydrogen gas (H_2) and a platinum catalyst to generate atomic hydrogen (H) in the gas phase.¹⁵ H appeared to etch graphite and other C allotropes, and investigation into the reaction of H with graphite by another U.S. group, E. A. Gulbransen *et al.* showed significant reaction rates that were largely independent of gas flow and pressure.¹⁷ Research into the role of H in low-pressure diamond synthesis came in 1966 from J. J. Lander and K. Morrison in the U.S., and independently B. V. Spitsyn *et al.* in Russia.^{16,18} It was revealed that in the presence of H_2 , the surface of the lattice became H terminated, preventing structure reformation and improving diamond yields.¹⁸ The following year, J. C. Angus *et al.*, a prominent group in the U.S., published findings that the observed graphitic etching was due to the relatively high reaction rates between H and graphite, when compared to H and diamond.¹⁹ When passing H_2 over HPHT diamond at 1033 °C and 50 atm H removed over 99% of graphitic C.

The early successes in metastable synthesis had been beset by poor diamond deposition rates.⁸ By the 1980s, initial teething problems with CVD development had been overcome and significant diamond growth rates were achievable.⁴ In 1981 B. V. Spitsyn *et al.* published establishing results of crystal growth on the scale of 10 μm onto foreign surfaces, opening up CVD to non-diamond substrates.²⁰ During this decade a number of different CVD techniques were also established, though they all largely relied upon the same key characteristics of CVD diamond growth. The C source is typically methane gas (CH_4), diluted in H_2 . The gas mixture is activated to instigate the dissociation of H_2 into H and the subsequent formation of reactive C species.²¹ The method of activation is essentially where techniques differ; the prominent methods in CVD are hot-filament (HF) reactors and plasma reactors. The modern era of CVD can largely trace its origins to Japan and the initial HF reactors were developed by Japanese researchers at the National Institute for Research in Inorganic Materials (NIRIM) in 1982.^{15,22} HF reactors share the necessity with plasma reactors for pressure and gas flow control, however require an electrical filament, typically made of a relatively inert metal such as tungsten (W) to reach minimum temperatures of 2200 °C.⁴ The electrical filament will have a limited lifetime; despite their relatively unreactive nature they will eventually react with input gases reducing their own resistivity and contaminating the grown diamond.

Contrastingly, plasma reactors involve a method of electrical discharge to strike a plasma and activate the gas phase; the favoured means of plasma-activation amongst CVD research since

before the turn of the millennia has been microwaves. Microwave Plasma CVD (MWPCVD) offers a number of advantages over other methods of CVD including higher growth rates and a large variety of gas compositions.⁴ The improved growth rates arise from the MWPCVD capability to maintain a higher local gas temperature (T_{gas}) across the larger volume of the reactor, however there will also be a large temperature gradient exhibited as T_{gas} falls to near room temperature at the relatively cool walls of the reactor.²³

Research into CVD at NIRIM resulted in the development of the first MWPCVD reactors in 1983, shortly after the HF reactor.²⁴ These consisted of a silica discharge tube designed to couple 2.45 GHz microwaves. Since then, there have been two variations of reactor in predominance; the NIRIM type reactor (figure 1.3a) and the Applied Science and Technology Inc. (ASTEX) type reactor (figure 1.3b), both of which couple microwaves into the substrate chamber to create a stable plasma above the substrate surface.⁴ Devised significantly later than the NIRIM type in 1998, the ASTEX type was jointly developed by Bachmann and ASTEX to allow for larger diameter substrates amongst other variations.²⁵ There have been numerous varieties of substrates considered for diamond growth, and it is often typical to grow diamond onto a pre-existing diamond surface to encourage mono-crystallinity in the new layers in order to obtain diamond's desired properties to a greater extent.²³ Promotion of homoepitaxial growth, that is the continuation of a crystal grain with the same orientation as the growth surface, is dependent on a number of growth conditions, notably variation in the C/H ratio and T_{gas} , and results in a higher concentration of H in the final film.^{21,23} Single crystal diamond (SCD) is preferential over polycrystalline diamond (PCD) for high quality diamond applications; optics, high energy beam detectors and thermal management, which require the exhibition of ideal diamond properties.²⁶

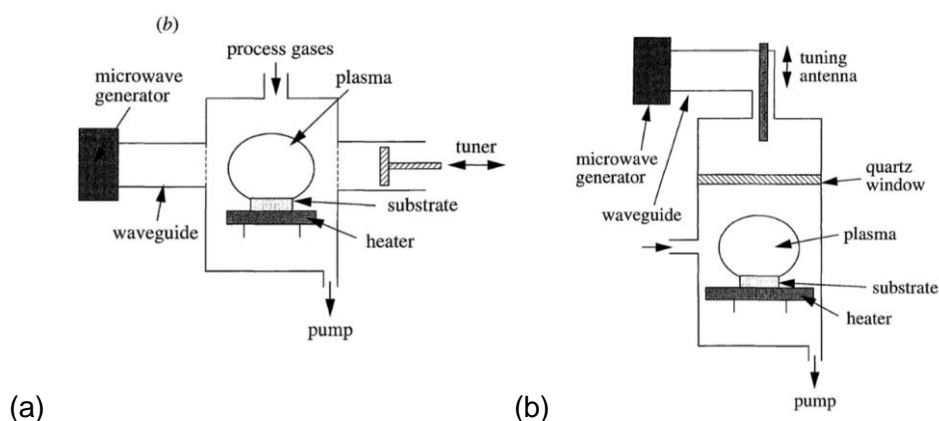


Figure 1.3: a) 'NIRIM type' and b) 'ASTEX type' MWPCVD reactors.⁴

As research into CVD, and notably MWPCVD, came through the turn of the millennia more commercial applications became practical and feasible on industrial scales. The applications of synthetic diamond, specifically CVD diamond, will typically reflect the exploitation of a particular desired property.⁴ In May 2018, the De Beers Group, one of the largest diamond miners and traders launched jewellery brand 'Lightbox' which champions their CVD SCD grown by De Beers off-shoot company Element Six.²⁷ Element Six has shared ties with synthetic diamond research since the 1950s and their CVD (and HPHT) PCD has found use in tooling for the oil and gas, automotive and aerospace, and mining and construction industries, as well as their SCD in precision technologies; thermal management, optics and consumer electronics.²⁸ A considerable number of these applications rely upon CVD diamond growth onto non-diamond substrates.

The growth of diamond onto a non-diamond substrate requires materials that show desirable behaviour at the high substrate temperature (T_{sub}) exhibited; the substrate will reach conditions exceeding 700 °C.⁴ For this reason materials with low melting points or coefficients of thermal expansion significantly different to that of diamond are not suitable for adherent diamond growth. Notably the latter of the two properties may be employed to encourage delamination of the newly grown diamond to form freestanding diamond. More often than not it is the preference to form diamond that does adhere to the substrate and subsequently silicon (Si), tungsten (W) and molybdenum (Mo) are common choices of substrate material, partially due to their ability to form carbides. A material capable of forming carbide layers; covalent bonding between C and the lower electronegativity element of the substrate offers significantly adherent diamond films and higher nucleation rates than other feasible materials such as copper and silver.^{4,25} It is noteworthy that unlike growth onto a pre-existing diamond surface, non-diamond surfaces promote heteroepitaxial growth resulting in PCD; divided into micro-, nano- and ultrananocrystalline diamond based on grain size.²⁶ Consequently such materials are normally pre-treated through abrasion or ultrasonic agitation with diamond grit to encourage nucleation sites.⁴

Concerns over T_{sub} are not limited to material selection, but also play a significant role in the growth of diamond on the substrate surface. T_{sub} is largely determined by the proximity of the plasma, the subsequent balance of gas heating and cooling, and the heat transfer to the reactor baseplate.²⁹ H₂ rich plasmas exhibit both a high heating rate and enhanced heat conduction, due to the higher thermal conductivity of H₂ gas. Substrate heating occurs from thermal conduction flux between the gas phase and surface, and by a smaller contribution the incident flux of H between the surface and the gas phase, determined by the near surface number density, [H]. The substantial role of the substrate in diamond growth has been suggested, and there are potential benefits arising from any significant ability to control T_{sub} .²³ In a purpose-built reactor with specific substrate heating and cooling system that may be possible. A more imprecise way of varying and controlling T_{sub} can be achieved by placing a thin wire coil below substrate. The gas gap created by the addition of the wire spacer will reduce thermal contact with the baseplate, and by varying the wire diameter (d_{wire}), T_{sub} may be adjusted.

1.3.1 Gas Phase Chemistry

As part of this study, the H and H₂ component of plasmas will be probed spectroscopically, to gauge the impact of variations in process conditions on the gas phase chemistry. In order to do this, it is necessary to review the current understanding of MW activated H and C/H plasmas studied in the relevant ASTEX type reactor.

As indicated, H plays a significant role in the gas phase chemistry of CVD diamond, and the dissociation of the diatomic to the monatomic form is key to this. So crucial is the presence of H that practical gas mixtures for diamond growth may contain less than 1% C species, C_xH_y to 99% H₂ by volume flow.³⁰ H is present on the diamond surface as points of lattice termination, stabilizing the surface and limiting graphitic rearrangement, and these terminating H atoms undergo abstraction by gaseous H atoms leading to the creation of radical sites on the surface.^{21,23} Despite adsorption of H from the gas phase reforming the terminal C-H bond in most cases, occasionally the radical site will chemisorb a C-containing radical to form an sp³ bonded C.²³ Thus the rate of formation of the diamond lattice is partially dependent on [H] at the substrate surface, and subsequently higher near surface [H] will promote faster diamond growth in the presence of a C source.³¹ The renewal of terminating species spurs overall dehydrogenation, the addition of new C atoms to the surface, the reaction of H with sp and sp² C sites and the net growth of the sp³ diamond surface. As discussed H will also

preferentially etch non-diamond sites into the plasma.²³ Terminating H atoms in help diamond maintain the sp^3 bonding, whereas in graphite the introduction of H disturbs the bonding in the graphite ring.⁷

While it is important to recognise the role of H is fundamental in the efficient deposition of diamond, plasmas made up of solely H offer insight into the processes taking place in the gas phase. There are two primary methods of formation of H from H_2 ; electron impact (EI) excitation and dissociation shown in equations 1a and 1b, and thermal dissociation (TD, equation 2) involving a third body M, where $M = H$ or H_2 . At low pressure (p), initial striking conditions, EI is favoured leading to H_2 triplet states and subsequent dissociation, at higher p (> 100 Torr [$1 \text{ Torr} = \frac{1}{760} \text{ atm} = 133.322 \text{ Pa}$]) with a higher molecular collision frequency, T_{gas} is adequate to favour the TD of H_2 .^{21,23,32} Thus it has been shown that TD is the prevailing mechanism in plasmas cores of T_{gas} higher than 2500 K.³³ It is also noted that ionization of electronically excited H ($n = 3$) atoms (H^* , generated via EI excitation [EIE] of ground state H atoms, and shown in equation 3) leads to the formation and subsequent abundance of the trihydrogen cation, H_3^+ (equation 4). Furthermore, a recent study has highlighted an alternative excitation mechanism in the production of H^* and H_2^* states through near resonant energy transfer (equation 5), which provides an alternate route in the formation of H ($n = 3$) and $H_2(d)$ states, for example.³⁴ This coupling is not believed to impact the spatial distribution of these excited states in the plasma.



Axially, there is a T_{gas} gradient from the plasma to the substrate, illustrated in the false colour plot in figure 1.4b.²³ T_{gas} reaches almost 3000 K in the plasma core, falling to around 500 K near the reactor walls, approximately 6 cm from the substrate surface. There is also a decrease in T_{gas} at the substrate surface, which combined with diffusion to the surface contributes to the lower [H] seen above the substrate in figure 1.4c. The MW electric field, $|E|$ is at a maximum above the substrate surface, leading to preferential coupling to free electrons in that region with increased gas heating. Consequently the electron density (n_e) and [H] exhibit similar distributions, achieving maxima in the plasma core, up to a relatively low height above the substrate and declining sharply in density outside of this region. These plasma parameters characterise a reduced electric field, $|E|/N$ (where N is the particle number acting to scatter particles accelerating in $|E|$) and, ultimately, the electron energy distribution function (EEDF), which is the number of electrons per energy at a particular position in the plasma.

H is intrinsically involved in adsorption at the diamond surface and subsequent incorporation of new C atoms, provided C has been introduced to the plasma by suitable gas precursor. It is also noted that H termination is a key factor in sp^3 stability with added inhibition and prevention of the formation of other C allotropes or C_xH_y at the surface. It is clear then, despite H predominance in the plasma and gas phase chemistry it is the introduction of additional species, evidently C_xH_y as well as numerous others that maintain the majority of attention in CVD research.

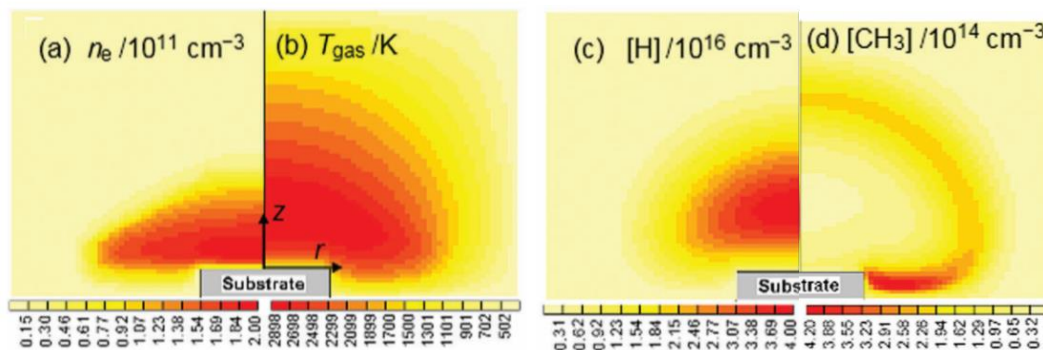


Figure 1.4 - Calculated 2-D(r, z) false colour distributions of a) n_e , b) T_{gas} , c) $[\text{H}]$ and d) $[\text{CH}_3]$ for a MW activated gas mixture comprising flow rates: $F(\text{CH}_4) = 25$ standard cubic centimetres per minute (sccm), $F(\text{Argon}) = 40$ sccm, $F(\text{H}_2) = 500$ sccm, operating at $p = 150$ Torr and with MW power = 1.5 kW. The model assumes cylindrical symmetry, a reactor radius, $r = 6$ cm and height, $h = 6.2$ cm, and a substrate diameter of 3 cm.²³

In conventional diamond CVD plasmas, that is H/C containing plasmas, reversible H-shifting reactions occur in the hottest regions and lead to the formation of C_xH_y , where integer values $x = 1, 2$ and $y \leq 3x$ (figure 1.5).^{21,23} Presently it is observed that upon incorporation of C_xH_y to the gas phase the distribution of the $[\text{CH}_3]$ in figure 1.4d contrasts that of $[\text{H}]$.²³ Subsequent recombination of C species in the cooler parts close to the reactor walls drives the reformation of CH_4 and heavier C_xH_y . The incorporation of low percentages of C_xH_y into the input gas does not drastically effect the spatial distributions of the charged species present barring H_3^+ , which will be succeeded by C_2H_2^+ and C_2H_3^+ . The n_e distribution will reflect the ionisation of C_2H_2 and recombination of electrons with C_2H_y^+ , lower ionisation energies increase n_e and reflect the distribution of T_{gas} and $[\text{H}]$ in the plasma core.²³ Despite its abundance at the reactor walls H_2 remains the dominant species in the plasma core, and the effect of T_{gas} promoting the conversion of CH_4 to C_2H_2 means that regardless of the numerous ionisation reactions and thermomdiffusion of neutral species to reactor walls the core is only weakly ionised.

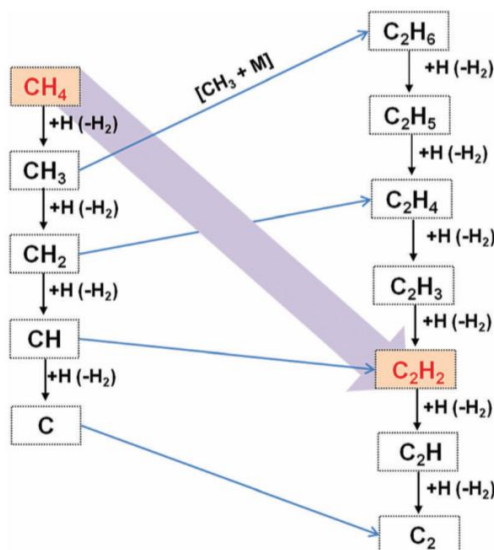


Figure 1.5 – H shifting reactions leading to formation of C_xH_y where integer values $x = 1, 2$ and $y \leq 3x$ in high T_{gas} and $[\text{H}]$.²³

The distributions of abstracted C_xH_y radicals such as C_2 , C_2H , CH and CH_3 can be measured by absorption spectroscopy techniques, and show correlations with high T_{gas} , therefore higher $[\text{H}]:[\text{H}_2]$, leading to elevated concentrations in the plasma core for all except CH_3 , itself showing a broader distribution with increased concentration at the core fringe and near the substrate (figure 1.4d).²³ This distribution agrees with the notion that CH_3 is the primary C_xH_y for incorporation into the diamond surface. Experimental data and plasma modelling reveals that in a H/C plasma, CH_3 has the largest number density of any C radical species close to the substrate, with near surface $[\text{H}]$ and $[\text{CH}_3]$ playing equally substantial roles as T_{sub} in regards to diamond growth.^{21,23} Contrastingly, CH_4 as with H_2 will be most

abundant in the periphery of the reactor, near the gas inlets. C_2H_2 notably is also in its highest number densities at the cold reactor walls, reflecting thermodiffusion with T_{gas} , although $[CH_4]$ remains higher than $[C_2H_2]$ due to the H-shifting recombinations.²³ $[C_2H_2]$ becomes larger than $[CH_4]$ as you move towards the plasma core, due to increasing H-shifting reactions with T_{gas} , and subsequently over 97% of C_xH_y in the plasma are C_2H_2 .

It is clear there is a vast array of chemistry and physical processes involved in the gas phase of a MWPCVD reactor, and a suitable solution to accommodate this and rationalise experimental results is to use theoretical modelling.^{23,35,36,37} It is important to note that due to the extensive number of processes taking place a model will require simplifications of some manner, for example the cylindrical nature of many reactors justifies the use of a 2-D coordinate system in height above the substrate (z) and radius (r). The Bristol-Moscow collaboration²³ generates such 2-D models, displayed in figure 4, specifically of H-based plasmas and the distribution of species as described. The definitive large, symmetrical temperature gradient is evident in the model of T_{gas} ; in excess of 3000 K in the core and falling to near room temperature at the walls of the reactor.²³ T_{gas} has been noted to directly affect the distribution of chemical species in the plasma as with the equilibrium of C_xH_y species. When modelling a H/C plasma a large number of neutral and charged species must be accounted for, including their relevant interactions and reactions.²³ This is only complicated further by the introduction of additional species to the plasma.

1.4 Dopants and Additional Species

A dopant is defined as “an impurity added to a pure substance to produce a deliberate change”.³⁸ Thus the introduction of C_xH_y to H_2 plasmas in relation to diamond growth is not strictly doping, and the H/C plasma is more representative of the CVD standard process. There are however, a number of species that are introduced into the CVD process to act as a dopant in the deposited diamond including boron (B), nitrogen (N) and oxygen (O).²³ The concept of their addition, as inferred by the use of the term dopant is to bring about alternative properties in the synthesised diamond. The use of dopants in chemistry is strongly linked to the introduction of semi-conduction to a material, and the same is true for diamond in regards to n-type and p-type doping. Diamond itself is an indirect band gap, intrinsic semiconductor sharing a measure of electronic similarity with the group IV metalloids Si and germanium (Ge).³⁹ Diamond has a wide enough band gap to render it largely insulating but, as with Si and Ge, it may be doped to form extrinsic semiconductors. Dopants are categorised into donors - elements with a valency greater than that of the material being doped - and acceptors, which have a lower valency. These respectively form n-type and p-type semiconductors due to the negative and positive charges they introduce to the doped material.

As additional species (X) are introduced to the plasma it remains important to consider the gas phase processes at work; just as the dominance of H_2 and its chemistry is evident in a H/C plasma, new species should be considered as additions to the H plasma. A knowledge of H/X chemistry is therefore required prior to understanding H/C/X plasmas in order to control doping. B is an example of a p-type dopant, and may be introduced to the gas phase in the form of diborane (B_2H_6).²³ Adding B_2H_6 shows insignificant changes to the plasma chemistry with B species concentrated at the core and near the substrate surface. For completeness, we note that it is also possible to incorporate B through ion-implantation; direct embedding of B ions through the diamond surface.⁴⁰ B-doped CVD diamond has been shown to impart semi-conductive and super-conductive properties to an otherwise insulating material.^{7,23,40,41} Potential n-type dopants in diamond include phosphorus (P) and N; forming reliable n-type doped diamond semiconductors proves difficult with P-doped diamond generating the most convincing results.⁴² H based plasmas contain a level of N impurity in the input gas, due to

variations in gas quality grades and air contamination, subsequently it is unfeasible not to find some level of N-doping in CVD diamond.^{23,43,44} In CVD the presence of N in low concentrations has been shown to increase the diamond growth rate and to favour {100} over {111} faceted growth, however higher concentrations have also correlated to a decrease in diamond quality.⁴⁴ Molecular N, N₂, remains stable and relatively abundant in the plasma core upon introduction to MWPCVD, with reactive N species concentrated to the diamond surface and concentrations of N₂ in the input gas only marginally altering the H/C gas phase chemistry and composition.²³

N may exist in diamond in the form a N-vacancy (NV) centre; a N and a vacancy replace two neighbouring C atoms, known as a split-vacancy configuration in the diamond lattice. This is an example of a single photon source (SPS) with applications in quantum information processing.⁴⁵ As the name implies a SPS is a light source that generates a quantum state of radiation containing a single excitation. This results in a purely electronic, non-phonon assisted sharp and intense emission between the lowest excited state and the ground state centred at a single λ , known as a zero-phonon line (ZPL).⁴⁶ NV centres are readily available in SCD and PCD, however a NV defect will exhibit a broad luminescence due to strong phonon-coupling, with a ZPL and phonon side-bands contributing to a feature width of approximately 100 nm at room temperature.^{45,47} Si may also exist in the form of an SPS in both synthesised and natural diamonds, as a Si-vacancy (SiV) centre, and these vacancies show potentially superior applicability to the NV centre in quantum technologies.^{45,48} SiV has a weak electron-phonon interaction compared to NV; a SiV centre shows a narrow band of less than 5 nm through a well-defined ZPL at 737 nm at room temperature.^{45,47} SiV defects have been less actively studied than NV defects, and interest exists in both encouraging and removing them from grown diamond. Much like diamond, Si is an intrinsic semiconductor, however with a smaller band gap. Doped Si is the most common extrinsic semiconductor with heavy usage in modern electronics, however Si also offers an alternate route to Si-doped diamond like C as a dopant itself.

1.4.1 Silicon

As well as a potential dopant with applicable optical defects, Si is a common impurity in diamond and can originate from the quartz windows of the CVD reactor or the use of Si substrates. In both cases, etched Si can contaminate the gas phase. Etching from a surface will occur when in the presence of a plasma; as with diamond growth, species in the gas phase may chemisorb to a surface and subsequently react with or displace surface species, which upon desorption are lost from the material into the plasma.⁴⁹ In this manner Si, or any other semi-volatile species may be etched from a surface into the gas phase. H atoms are a prime offenders as an etching species and this is evident in their preferential etching of graphite over diamond.^{7,50} H based plasmas may therefore etch impurities into the gas phase, and subsequently deposit them in the diamond film. Understanding the incorporation and behaviour of Si in the gas phase chemistry is thus important if minimising or maximising the Si content of diamond is desired.

Si can be integrated into diamond through etching, as well as ion-implantation and incorporation in the input gas mixture.^{47,51} Silane (SiH₄) is a suitable Si containing gas that can be introduced to H/C mixtures. It has been noted that increasing SiH₄ concentrations to encourage high level Si doping can also promote non-diamond C growth.⁵² H/C/Si plasmas are therefore of significant interest for reliably producing semi-conducting diamond and SiV centres in CVD diamond. To develop a correct understanding of H/C/Si plasmas, however, H/Si plasmas must be understood first. Emission from the SiV defect is detectable at 737 nm, thus the presence of silicon in the diamond film is detectable spectroscopically, though other

methods must be used to monitor Si in the gas phase.⁵³ Emission spectroscopy offers a solution to this issue; Si emits through its $3s^23p4s \rightarrow 3s^23p^2$ transition, and SiH radicals through the $A^2\Delta \rightarrow X^2\Pi$ transition. Si and SiH emission have been previously investigated by Alim Lalji, however the gas phase processes in H/Si plasmas remain elusive.⁵⁴ Ground state Si atoms absorb through their triplet to triplet transitions at approximately 250 nm which encourages investigation through absorption spectroscopy.

1.4.2 Argon

In contrast to dopant species, Argon (Ar) is an additional input gas that appears to show neither incorporation into the diamond film nor to significantly perturb of the gas phase, barring a few changes.⁵⁵ The presence of Ar in a H/C plasma may increase η_e in the plasma, raise T_{gas} and electron temperature (T_e), and slightly alter the diamond film morphology; promoting {100} facet growth, high sp^3 character and low defect crystallinity.^{29,32,56} MWPCVD models also suggest increasing Ar concentrations encourages EI dissociation of H_2 and C_2H_y species, leading to higher overall levels of dissociation in the plasma with increased [H] and $[C_2]$, which likely links with the observed increases in growth rates.^{7,32,57,58} Ar effectively replaces H_2 in the plasma, reducing the overall MW power absorbed by rovibrational excitation of H_2 , resulting in the expansion of the plasma itself with a lower, more homogenous power density.^{29,57} The resulting Ar rich plasmas exhibit a much reduced thermal conductivity, due to the higher mass of Ar and thus affect the conductive heat flux to the substrate.²⁹ Total substrate heating increases by approximately 10 times from Ar rich to H_2 rich plasmas, however substrate cooling is similarly significantly reduced, notably by decreased conductive heat transfer in the gas gap between the substrate and the reactor baseplate.⁵⁹ Increasing the Ar fraction increases T_{sub} , until a maximum T_{sub} is found at an H_2 :Ar ratio of approximately 20:80, where Ar and H_2 show comparable conductivity, however there remains room for further investigation into the effect of Ar on T_{sub} . Ar emissions are detectable by emission spectroscopy and used as an inert tracer species in small, known quantities for actinometry to deduce species concentrations in comparison to Ar.⁶⁰ Ar addition offers the potential for increased growth rates and hotter plasmas without significant effects to the diamond grown, and its involvement with substrate temperature and thermal conductivity will be investigated in this report.

1.5 Spectroscopic Methods

The deductions leading to these descriptions of gas phase activity came in part from modelling and spectroscopic observations.³¹ There are a large number of techniques researchers have employed to analyse the CVD gas phase chemistry including but not limited to Optical Emission Spectroscopy (OES),^{57,60} Cavity Ring Down Spectroscopy (CRDS),^{32,61,62} Resonance-Enhanced Multiphoton Ionization (REMPI),^{63,64} Mass Spectroscopy (MS)⁶⁵ and Molecular Beam Mass Spectroscopy (MBMS),^{66,67,68} Infrared (IR)⁶⁹ and Raman spectroscopy,^{7,56,70,71} and numerous specialised spectroscopic methods.⁵⁶ From the initial work carried out in this thesis OES and CRDS were highlighted as practically relevant techniques, and both have been employed to probe the gas phase chemistry of MW activated H-based plasmas.

1.5.1 Optical Emission Spectroscopy

OES is the primary non-invasive analytical technique employed in this work, and offers detection of key emission lines in H based plasmas, notably the $d^3\Pi_u \rightarrow a^3\Sigma_g^+$ (Fulcher) transition in H_2 and transitions of atomic H terminating on the $n = 2$ (Balmer series).^{34,59} OES is a fairly simple and practically convenient technique that typically detects products of EIE, without perturbing the plasma itself. It may therefore be used as a probe of T_{gas} , n_e , EEDFs

and associated T_e , which are difficult to quantitatively determine.⁵⁷ OES has been used with this MWPCVD reactor set up on a number of occasions to identify excited H, H₂, CH and C₂ species, and excited states of various dopant species. Such an investigation may vary process conditions including but not limited to; MW power (P), p , gas flow, substrate diameter (d_{sub}), and d_{wire} .^{34,59} Recent work with this set-up found that H₂* emissions provide a sensitive probe of the hyper-thermal component of the EEDF; energies ≥ 10.2 eV above the ground state.³⁴ A full description of the EEDFs are needed to reliably model plasmas, and subsequently there is room for further investigation into the thermal component with energies < 10.2 eV. In this study, Mahoney *et al.* also identified the near-resonant excitation transfer reactions illustrated in Section 1.3.1, equation 5 as an alternative source of H ($n = 3$) and H₂(d).³⁴ Another study in this reactor identified emission from C₂* species arising from dissociative electron attachment (DEA) to C₂H radicals, and suggested the densities of these C anions may support the use of a positive substrate bias, which is predetermined direct electrical current applied to the substrate.⁵⁷

In conventional plasmas, the presence of C₂* radical species can be monitored through the C₂ Swan band ($d^3\Pi \rightarrow a^3\Pi$ transition).⁵⁵ These species are indicative of total C content and may be cast in the form of Boltzmann plots that provide a measure of the species rotational temperature and thus, given the high collision frequency, T_{gas} . In a similar manner the emissions of Si were monitored to provide insight into Si content within the reactor.⁵⁴ Spectral analysis of OES further affords the ability to calculate spatial distributions; variance in emission as a function of z . In an EI dominated plasma environment, the optical emission intensities represent a convolution of the spatial distributions of the ground state species of interest and of suitably energetic electrons. Amongst other extractions, OES offers instant insight into the behaviour of gas species without altering the reactor itself, and may be used in combination with variations process conditions, as a result it is of great practical advantage to MWPCVD investigation.

1.5.2 Cavity Ring Down Spectroscopy

CRDS is another method of analysis available to probe species within the reactor, and most notably offer absolute column density measurements of these species in specific quantum states. "CRDS is an ultrasensitive multipass absorption technique"³² that has been employed in many CVD studies, often complementary to OES in DC arc jet and MWPCVD reactors. Once again species such as C₂ can be investigated without disturbing the gas phase chemistry alongside alterations in p , P and other process conditions. CRDS relies upon trapping a laser pulse in an almost completely reflective linear cavity; two mirrors of approximately 99.9% reflectivity which transmit a small fraction of detectable light through allowing for the measurement of the decay of light intensity within the cavity, and hence the absorbance.⁷² The detected intensity (I_t) is related to the initial intensity (I_0) by the detection time (t) and the ring-down lifetime (τ) through equation 7.

$$I_t = I_0 e^{-t/\tau} \quad (6)$$

Knowledge of τ for an empty cavity and with a plasma present allows for determination of absorbance (A), and furthermore the column number density provided knowledge of the absorption cross-section and path length, and suitable laser bandwidths and modes are employed. Difficulty lies in the inhomogeneous nature of the cavity in CVD where T_{gas} may vary by an order of magnitude across the reactor. Through combining quantitative column densities with gas phase modelling it is possible to extract out and predict species distributions in a CVD reactor.³²

1.6 Aims

The main investigations in this thesis involve the use of OES and CRDS to determine the state of H based plasmas. The primary use of OES will be to probe H_{α} and $H_2(d-a)$ emissions under varying process conditions in an effort to investigate T_{sub} control. The intention is to demonstrate the impact of Ar, d_{sub} and d_{wire} have on the gas phase and surface processes, and their influence on T_{sub} . These concepts of these variables have been introduced in this section, however will be discussed in further detail in the following sections. H_{α} and $H_2(d-a)$ both act to probe the hyperthermal component of the EEDF. This has been demonstrated in previous work and H emissions have been used in other studies to estimate T_e from the emission line intensities. It is the intention to also exhibit this sensitivity to the hypothermal component, however in order to examine the thermal component of the EEDF, an alternative species is needed.

The secondary use of OES involves the introduction of Aluminium (Al) into the gas phase in an effort to probe the thermal component of the EEDF and subsequently T_e . As with Si, the phenomena of etching opens opportunities to introduce unlikely species into the gas phase that would be difficult to incorporate in the manner of common dopants and impurities. Plasma etching is commonly used to incorporate metal elements into the gas phase.⁴⁹ In this manner it is hoped that Al may be integrated in H based plasmas, and subsequent Al emissions be used to probe EEDFs. We know that OES is capable of detecting emissions from excited species within the plasma and indirectly examining the EEDFs to measure η_e and T_e amongst other quantities.⁷³ Etching of Al and Aluminium Oxide (Al_2O_3) has been shown with halogen based etchants, and notable sputtering prior to etching results in a higher etching rate.⁷⁴ It is therefore probable that an Al based substrate in the presence of a H based plasma would undergo some level of etching. Al has also been introduced into the gas phase through laser irradiation and evaporation methods, both of which allow for the detection of excited Al species by OES and hopefully insight into the thermal component of the EEDFs.^{75,76} In the case of introducing an additional substrate to the reactor the effect of plasma conditions on the substrate must be noted, most significantly the resulting T_{sub} . In the case of Al its melting point is approximately 660 °C, which falls dangerously close to the typical T_{sub} in a MWCVD reactor, and for this reason Al_2O_3 has also been considered.⁷⁷

Gas phase processes may then be studied as a function of substrate temperature and T_e , with potential insights into etching control in regards to substrate temperature. The use of CRDS will also be used to investigate the incorporation of Si into the gas phase through SiH_4 under varying process conditions. The experimental work is intended to contribute to the understanding of MW H/Si and H/C/Si plasma chemistry, beneficial to the incorporation or removal of Si in diamond. The presence of Si as both an impurity and SiV centre justifies the appeal in developing a working knowledge of Si doped MW plasmas, and combined with computational modelling and additional studies will address the insufficiency in the current understanding. The Si will be reported as a column density through the plasma at a known z , and measured through three absorption transitions of Si atoms. The objective is to arrive at some comprehension of the behaviour of Si, and indirectly SiH_4 in the gas phase as a response of variations in process conditions.

1.7 References

1. Paul Ziminisky Diamond Analytics 2016, <http://www.paulziminisky.com/2016-global-diamond-production-by-mine>, (Last accessed October, 2018)
2. D. W. Olson and A. S. Bricche, *Minerals Yearbook: Diamond, Industrial*, U.S. Geological Survey, United States, 2015
3. D. Choudhary and J. Bellare, *Ceram. Int.*, 2000, **26**, 73-85
4. P.W. May, *Phil. Trans. R. Soc. Lond. A*, 2000, **358**, 473-495
5. J. E. Field, *Rep. Prog. Phys.*, 2012, **75**, 126505-126540
6. J. Robertson, *Mater. Sci. Eng. R*, 2002, **37**, 129-281
7. J. J. Gracio, Q. H. Fan and J. C. Madaleno, *J. Phys. D: Appl. Phys.*, 2010, **43**, 374017-374039
8. J. C. Angus and C. C. Hayman, *Sci.*, 1988, **241**, 913-921
9. S. Lee, D. Kang and J. Roh, *Carbon Lett.*, 2015, **16**, 135-146
10. C. Ye, B. Shentu and Z. Weng, *J. Appl. Polym. Sci.*, 2006, **101**, 3806-3810
11. A. K. Geim and K. S. Novoselov, *Nat. Mater.*, 2017, **6**, 183-191
12. F. P. Bundy, H. T. Hall, H. M. Strong and R. H. Wentorf, *Nature*, 1955, **176**, 51-55
13. H. P. Bovenkerk, F. P. Bundy, H. T. Hall, H. M. Strong and R. H. Wentorf, *Nature*, 1959, **184**, 1094-1098
14. M. Akaishi, *Diam. Relat. Mater.*, 1993, **2**, 183-189
15. J. C. Angus, *Diam. Relat. Mater.*, 2014, **49**, 77-86
16. B. V. Spitsyn, *J. Cryst. Growth*, 1990, **99**, 1162-1167
17. E. A. Gulbransen, K. F. Andrew and F. A. Brassart, *J. Electrochem. Soc.*, 1965, **112**, 49-52
18. J. J. Lander and J. Morrison, *Surf. Sci.*, 1966, **4**, 241-246
19. J. C. Angus, H. A. Will and W. S. Stanko, *J Appl. Phys.*, 1968, **39**, 2915-2922
20. B. V. Spitsyn, L. L. Bouilov and B. V. Derjaguin, *J. Cryst. Growth*, 1981, **52**, 219-226
21. J. E. Butler, Y. A. Mankelevich, A. Cheesman, J. Ma and M. N. R. Ashfold, *J. Phys.: Condens. Matter*, 2009, **21**, 364201-364221
22. S. Matsumoto, Y. Sato, M. Tsutsumi and N. Setaka, *J. Mater. Sci.*, 1982, **17**, 3106-3112
23. M. N. R. Ashfold, E. J. D. Mahoney, S. Mushtaq, B. S. Truscott and Y. A. Mankelevich, *Chem. Commun.*, 2017, **53**, 10482-10495
24. Y. Saito, S. Matsuda and S. Nogita, *J. Mater. Sci. Lett.*, 1986, **5**, 565-568
25. P. K. Bachmann and W. Enckevort, *Diam. Relat. Mater.*, 1992, **1**, 1021-1034
26. S. Nad, PhD Thesis, Michigan State University, 2016
27. LightBox, www.lightboxjewelry.com, (Last accessed February 2019)
28. Elementsix, www.e6.com, (Last accessed February 2019)
29. J. C. Richley, O. J. L. Fox, M. N. R. Ashfold and Y. A. Mankelevich, *J. Appl. Phys.*, 2011, **109**, 063307-063314
30. N. M. Hwang and D. Y. Yoon, *J. Cryst. Growth*, 1996, **160**, 98-103
31. J. E. Butler and R. L. Woodin, *Phil. Trans. R. Soc. Lond. A*, 1993, **342**, 209-224
32. J. Ma, J. C. Richley, M. N. R. Ashfold and Y. A. Mankelevich, *J. Appl. Phys.*, 2008, **104**, 103305-103309
33. A. Gicquel, K. Hassouni, F. Silva and J. Achard, *Curr. Appl. Phys.*, 2001, **1**, 479-496
34. E. J. D. Mahoney, B. S. Truscott, S. Mushtaq, M. N. R. Ashfold and Y. A. Mankelevich, *J. Phys. Chem. A*, 2018, **122**, 8286-8300
35. K. Hassouni, T. A. Grotjohn and A. Gicquel, *J. Appl. Phys.*, 1999, **86**, 134-151
36. B. S. Truscott, M. W. Kelly, K. J. Potter, M. Johnson and M. N. R. Ashfold, *J. Phys. Chem. A*, 2015, **119**, 12962-12976
37. K. Hassouni, A. Gicquel, M. Capitelli and J. Loureiro, *Plasma Sources Sci. Technol.*, 1999, **8**, 494-512
38. *Webster's New World College Dictionary*, Wiley, Indianapolis, IN and Chichester, 4th edn., 2004
39. D. A. Neamen, *Semiconductor Physics and Devices: Basic Principles*, McGraw-Hill Higher, New York, 3rd edn, 2003
40. R. Kalish, *Carbon*, 1999, **37**, 781-785
41. B. K. Xiang, D. W. Zuo, X. F. Li, F. Xu and M. Wang, *Key Eng. Mater.*, 2010, **426-427**, 30-34
42. K. Haenen, K. Meykens, M. Nesládek, G. Knuyt, L. M. Stals, T. Teraji, S. Koizumi and E. Gheeraert, *Diam. Relat. Mater.*, 2001, **10**, 439-443
43. B. S. Truscott, M. W. Kelly, K. J. Potter and M. N. R. Ashfold, *J. Phys. Chem. A*, 2016, **120**, 8537-8549

44. V. Baranauskas, B. B. Li, A. Peterlevitz, M. C. Tosin and S. F. Durrant, *J. Appl. Phys.*, 1999, **85**, 7455-7458
45. E. Neu, D. Steinmetz, J. Riedrich-Moeller, S. Gsell, M. Fischer, M. Schreck and C. Becher, *New J. Phys.*, 2011, **13**, 025012-025032
46. K. K. Rebane and I. Rebane, *J. Lumin.*, 1993, **56**, 39-45
47. V. S. Sedov, V. S. Krivobok, A. V. Khomich, V. G. Ralchenko, A. A. Khomich, A. K. Martyanov, S. N. Nikolaev, O. N. Poklonskaya and V. I. Konov, *J. Appl. Spectrosc.*, 2016, **83**, 229-233
48. C. M. Breeding and W. Wang, *Diam. Relat. Mater.*, 2008, **17**, 1335-1344
49. C. Cardinaud, M. Peignon and P. Tessier, *Appl. Surf. Sci.*, 2000, **164**, 72-83
50. P. Sukkaew, Ö. Danielsson, L. Ojamäe, *J. Phys. Chem. A*, 2018, **122**, 2503-2512
51. D. P. Hickey, PhD Thesis, University of Florida, 2007
52. V. Sedov, V. Ralchenko, A. A. Khomich, I. Vlasov, A. Vul, S. Savin, A. Goryachev and V. Konov, *Diam. Relat. Mater.*, 2015, **56**, 23-28
53. A. M. Edmonds, M. E. Newton, P. M. Martineau, D. J. Twitchen and S. D. Williams, *Phys. Rev. B*, 2008, **77**, 245205-245211
54. A. Lalji, Masters Thesis, University of Bristol, 2018
55. K. W. Hemawana and R. J. Hemley, *J. Vac. Sci. Technol. A*, 2015, **33**, 061302-061322
56. H. C. Shih, C. P. Sung and W. L. Fan, *Surf. Coat. Technol.*, 1992, **54-55**, 380-386
57. E. J. D. Mahoney, B. S. Truscott, M. N. R. Ashfold and Y. A. Mankelevich, *J. Phys. Chem. A*, 2017, **121**, 2760-2772
58. A. Tallaire, C. Rond, F. Bénédic, O. Brinza, J. Achard, F. Silva and A. Gicquel, *Phys. Status Solidi A*, 2011, **208**, 2028-2032
59. E. J. D. Mahoney, S. Mushtaq, M. N. R. Ashfold and Y. A. Mankelevich, *J. Phys. Chem. A*, 2019, **123**, 2544-2558
60. J. Ma, M. N. R. Ashfold and Y. A. Mankelevich, *J. Appl. Phys.*, 2009, **105**, 043302-043312
61. J. B. Wills, J. A. Smith, W. E. Boxford, J. M. F. Elks, M. N. R. Ashfold, and A. J. Orr-Ewing, *J. Appl. Phys.*, 2002, **92**, 4213-
62. E.H. Wahl, T.G.Owano, C.H.Kruger, Y.Ma, P.Zalicki and R.N.Zare, *Diam. Relat. Mater.*, 1997, **6**, 476-480
63. F.G. Celii and J.E. Butler, *Appl. Phys. Lett.*, 1989, **54**, 1031
64. F.G. Celii and J.E. Butler, *J. Appl. Phys.*, 1992, **71**, 2877
65. S. J. Harris and L.R. Martin, *J. Mater. Res.*, 1990, **5**, 2313
66. W.L. Hsu and D.M. Tung, *Rev. Sci. Instrum.*, 1992, **63**, 4138
67. C. A. Rego, R. S. Tsang, P. W. May, M. N. R. Ashfold and K. N. Rosser, *J. Appl. Phys.*, 1996, **79**, 7264
68. S. Park, F. Liao, J. M. Larson, S. L. Girshick and M. R. Zachariah, *Plasma Chem. Plasma Process.*, 2004, **24**, 353-372
69. T. Mitomo, T. Ohta, E. Kondoh and K. Ohtsuka, *J. Appl. Phys.*, 1991, **70**, 4532
70. S. J. Harris, *J. Appl. Phys.*, 1996, **80**, 2187
71. D. S. Knight and W. B. White, *J. Mater. Res.*, 1989, **4**, 385-393
72. U. Lommatzsch, E. H. Wahl, D. Aderhold, T. G. Owano, C. H. Kruger and R. N. Zare, *Appl. Phys. A*, 2001, **73**, 27-33
73. N. Derkaoui, C. Rond, T. Gries, G. Henrion and A. Gicquel, *J. Phys. D: Appl. Phys.*, 2014, **47**, 205201-205211
74. D. W. Hess, *Plasma Chem. Plasma Process.*, 1982, **2**, 141-155
75. P. Sankar, J. J. J. Nivas, N. Smijesh, G. K. Tiwari and R. Philip, *J. Anal. At. Spectrom.*, 2017, **32**, 1177-1185
76. I. Banerjee, N. V. Kulkarni, S. Karmaker, V. L. Mathe, S. V. Bhoraskar and A. K. Das, *Plasma Sci. Technol.*, 2010, **12**, 27-30
77. F. O. Jones and K. O. Wood, *Br. J. Appl. Phys.*, 1964, **15**, 185-187

2. Experimental

2.1 Microwave Plasma Chemical Vapour Deposition

2.1.1 Reactor

All experimental work undertaken for this thesis was carried out using a custom ASTEX type MWPCVD reactor (figure 2.1) to generate MW activated H plasmas.¹ The reactor operates MW powers at up to 2 kW, generated from a 2.45 GHz Muegee power supply.² The MW radiation is delivered into the reactor through a rectangular waveguide and a set of three tuning forks converting to the TM_{01} mode, coupling the MW into a standing wave within the reactor chamber.¹ The whole reactor chamber is a vertically aligned cylinder of inside diameter 12.0 cm, with a quartz window separating a lower deposition chamber of volume approximately 600 cm³.² This bottom chamber is vacuum sealed, and contains the substrate and the plasma when in use.¹ The substrate itself sits on an oxygen-free electronic-grade water-cooled copper sample stage mounted in an aluminium alloy reactor base plate.³ The top section is open to the atmosphere, and air is vented over the quartz window to keep it cool.

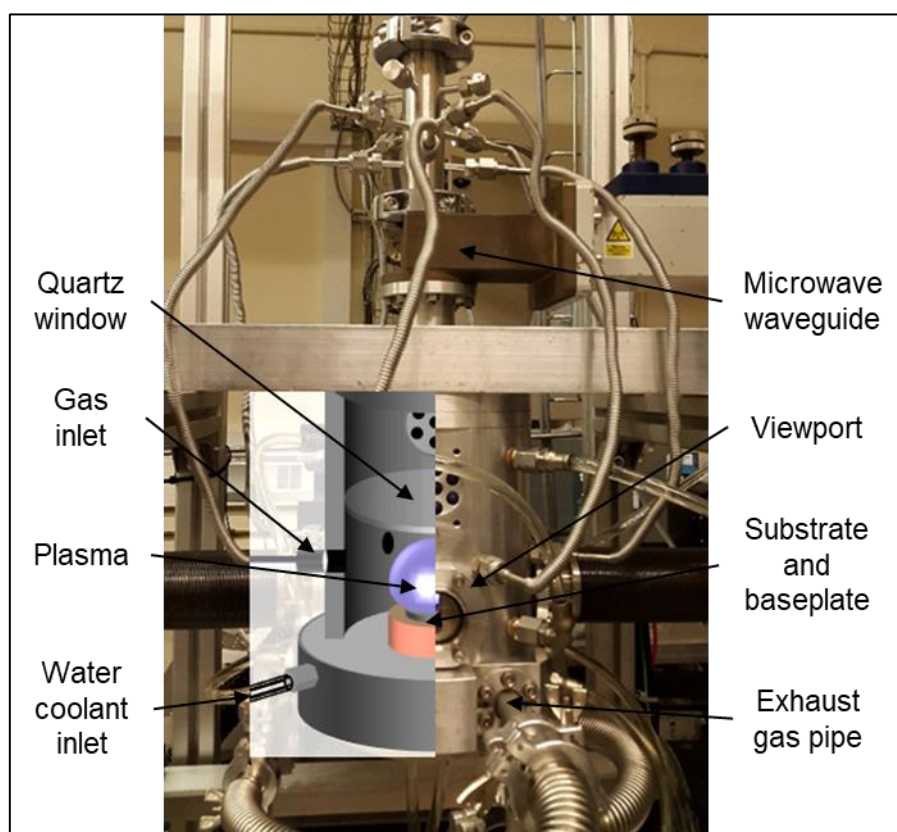


Figure 2.1 – The custom ASTEX type MWPCVD reactor, with an illustration of the internal components on the left half of the structure.

The source gases are metered separately to set flow rates in sccm through individual mass flow controllers (MFCs), then mixed and flowed through a single pipe to homogenise the input gas. The gas mixture is then evenly distributed through eight symmetrically positioned 4 mm inlet pipes below the quartz window, offering a cylindrical gas input into the reactor.^{2,3} The source gases are vented through the base plate. The microwaves coupled into the lower chamber will activate the gas mixture, generating the reactive species previously discussed.

Notably such plasmas are initially activated with a H_2 flow rate, $F(H_2) = 300$ sccm at $p \approx 15$ Torr and $P < 1$ kW, then brought to $p = 150$ Torr, $P = 1.5$ kW, usually defined as base conditions prior to the introduction of additional source gases. Typical experimental variations in p and P tend to be in the ranges of $0.7 \leq P \leq 1.85$ kW and $75 \leq p \leq 275$ Torr, and in most cases in this study performed by varying one parameter while maintaining the others at base values.³

2.1.2 Substrate Variables

MW activated H plasmas were used as the simplest system for investigating a control of T_{sub} , specifically through examining the impact of d_{sub} , d_{wire} and $F(Ar)$, and a combination of these on plasma uniformity and T_{sub} . As discussed in section 1.3, there are numerous materials available for use as a substrate in MWPCVD. Cylindrical W substrates, of thickness 3 mm and of varying $d_{sub} = 17$ mm and 32 mm were studied. It was also the case that on occasion the substrates were mounted axisymmetrically on an annular spacer composing of Mo wire, of varying $d_{wire} = 0.002''$, $0.004''$, $0.006''$, $0.008''$ and $0.01''$. These variables offered a significant impact on T_{sub} , with the latter affording a control over thermal conduction of the substrate and the copper stage discussed in section 1.3, and the subsequent variation in T_{sub} . In the case of examining the impact of d_{wire} , a W substrate of $d_{sub} = 17$ mm was used. In order to vary the substrate or spacer wire, the reactor must be brought to atmospheric pressure and the base plate removed. This justified the regular recording of leak rates and the limitation of substrate variations. For the OES experiments, reactor air leak rates were measured regularly by pressure rise from base vacuum and were found to be in the magnitude of 0.1 mTorr min^{-1} (approximately 1 parts per million, ppm at base conditions) on average. Where possible T_{sub} was measured using a one or two-colour pyrometer (700 - $1300^\circ C$), though these measurements may be altered near-IR H_2 emissions.⁴ Emissions from C species interfere with pyrometer measurements and CH_4 was not introduced into the input gas mixture of the majority of the plasmas studied.

Section 1.6 introduced the concept of integrating Al into the gas phase through etching. Two Al-based substrates were used; a square Al substrate of thickness 0.5 mm and $d_{sub} = 10$ mm and a square Al_2O_3 substrate of thickness 1 mm and $d_{sub} = 3.2$ mm. These were centred on top of the 32 mm W substrate, as depicted in figure 2.2a.

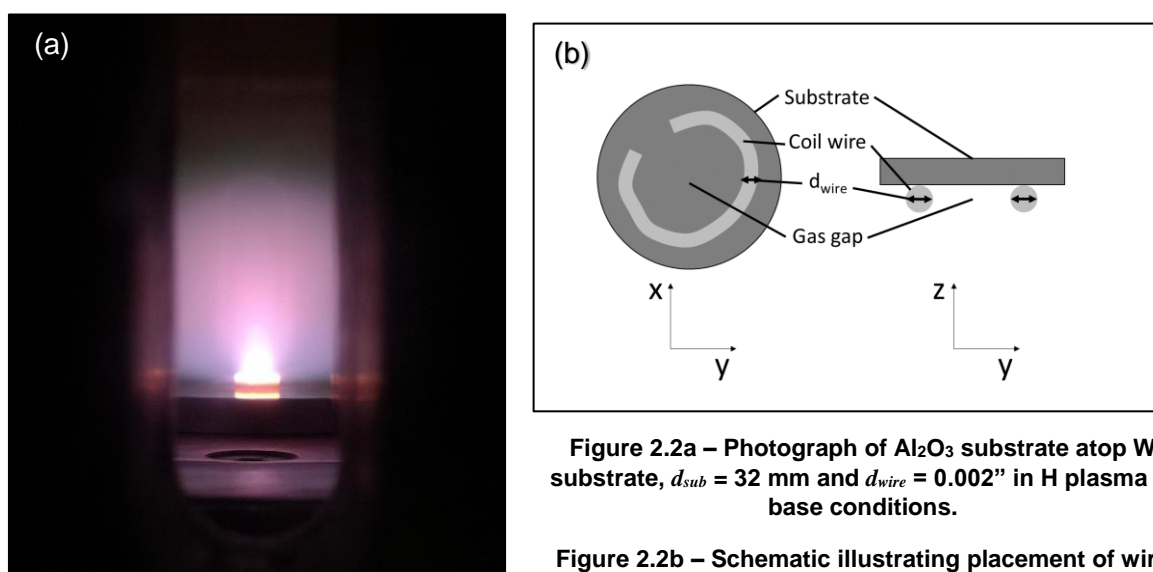


Figure 2.2a – Photograph of Al_2O_3 substrate atop W substrate, $d_{sub} = 32$ mm and $d_{wire} = 0.002''$ in H plasma at base conditions.

Figure 2.2b – Schematic illustrating placement of wire coil.

2.1.3 Addition of Argon, Silane and Methane

In the addition of Ar a number of $F(\text{Ar})$ were employed; $F(\text{Ar}) = 24$ sccm, 150 sccm, 200 sccm and 300 sccm. Variations in $F(\text{Ar})$ were made at constant P and p (1.5 kW and 150 Torr), and the plasma studied as a function of $F(\text{Ar})$. After any variation in process conditions the plasma was left to equilibrate for 6 minutes to ensure the plasma was close to steady-state.

Introducing SiH_4 into the input gas mixture required a MFC that allowed access to flow rates two orders of magnitude lower than other input gases. In the case of the CRDS experiments, at $F(\text{SiH}_4)$ as low as 1.0 sccm Si absorption would saturate, in other words at an effective input mole fraction of SiH_4 , $X_0(\text{SiH}_4) = 0.1\%$ of $X_0(\text{H}_2)$. Subsequently when measuring Si as a function of z , P and p , $F(\text{SiH}_4) = 0.5$ sccm was used with a $F(\text{H}_2)_{\text{total}} = 600$ sccm. H/Si was also studied with varying flow rates of H_2 , resulting in an decrease of $X_0(\text{SiH}_4)$ with increased $F(\text{H}_2)$. When altering $F(\text{H}_2)$ from the base 300 sccm, the time taken for the plasma to equilibrate was assumed to scale inversely. The leak rates for the CRDS experiments varied from that of the OES, due to the addition of the arm mounted mirrors and consequentially were on the order of 10 ppm. Thus it was the case that the $X_0(\text{gas}) > X_0(\text{SiH}_4)$, rather than the ideal $X_0(\text{gas}) \ll X_0(\text{SiH}_4)$

A $F(\text{CH}_4)$ was also introduced to form C/H/Si plasmas, at $X_0(\text{CH}_4) = 0$ to $X_0(\text{CH}_4) = 32.5$ ppt (parts per thousand), along with a compensatory decrease in $F(\text{H}_2)$.

2.2 Spectroscopy

As discussed in the section 1.5, two methods of spectroscopy; OES and CRDS have been highlighted and implemented in the study of H-based plasmas for this study. The reactor is equipped with four, exchangeable port holes that offer vertical slot-shaped quartz viewports or the capability of attaching side-arms to the reactor. Through these ports OES and CRDS offer non-invasive insight into the populations and distributions of reactive species within the gas phase.

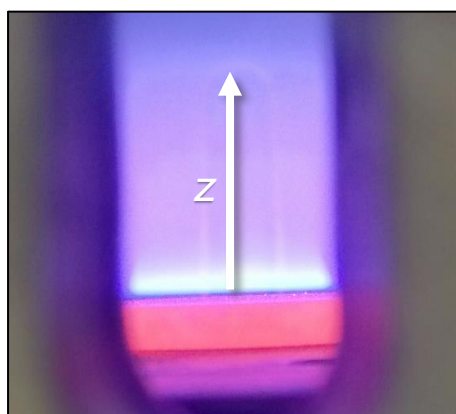
2.2.1 Optical Emission Spectroscopy

OES was carried out using a Czerny-Turner spectrograph (Andor SR-500i) with a 500 mm focal length $f/16$ objective lens. Emissions from the plasma pass through the back facing vertical reactor viewports and through the 10 μm width entrance slit into the spectrograph. Within the spectrograph the radiation is reflected and collimated, diffracted by a choice of gratings and focused onto a Charge Coupled Device (CCD) array detector. The diffraction gratings defined the λ range observed; gratings 1 and 2 offering a range of 142 nm and 72 nm respectively, with the latter yielding a higher resolution. The diffracted λ are detected by the CCD detector (Andor Newton 950), which is cooled to -60 °C to remove background radiation and limit pixel saturation. The lens is focused on the centre of the chamber and aligned with the vertical viewport in order to image the middle of the plasma. The small lens aperture assumes emission from the entire depth of plasma and the choice of diffraction gratings offers a variety of λ ranges and resolutions. The front viewport was covered during measurement taking and external lighting removed to further limit background noise. Exposure and number of accumulations were varied in response to CCD saturation, but in each experiment total accumulation time was aimed to be maintained.

Andor Solis software was used to record the OES output and offered instantaneous imaging of each emission capture. This allowed for immediate verification of emitting species and any

saturation of the CCD. The spectral y-axis is defined as height above the substrate, z from spatial calibration, and the x-axis as λ , which may be converted from pixels through a polynomial expression. Spectra are spatially calibrated through imaging alternating black and white scale on the centre of the copper stage at the same settings used for experimental imaging. The black and white spatial target is defined by alternating 3 mm bars, and the relative height above the substrate is taken as $-3 \leq z \leq 27$ mm, where $z = 0$ mm is defined as the substrate surface.⁵ From the imaged black and white scale, the coordinates, z and λ of the full height are noted in pixels, and used to de-skew the experimental spectra in the computational program MATLAB. MATLAB was also used to produce spatial profiles or spatial distributions of the relevant emission peaks; a plot of the intensity of emission relative to the height above the substrate. Multiple spatial profiles may be plotted together to illustrate a change in emission as a function of plasma conditions.

The relevant emissions for H were the Balmer series, showing prominently at 410.2, 434.1, 486.1 and 656.2 nm for transitions to $n = 2$ at approximately 10.2 eV from $n = 6$, $n = 5$, $n = 4$, and $n = 3$ respectively.^{6,7} H_2 was monitored via the $d^3\Pi_u \rightarrow a^3\Sigma^+_g$ transition. These transitions are defined explicitly in figure 2.4, with the observed λ , upper state energy, electronic transition and Einstein A coefficients, A_{ki} given. Al shows strong emissions at 308.22 nm and 309.27 nm, and 394.40 nm and 396.15 nm due to $3s^23d \rightarrow 3s^23p$ and $3s^24s \rightarrow 3s^23p$ transitions respectively, and these emissions are discussed in more detail in a later section.^{7,8}



	$\lambda_{\text{obs}} / \text{nm}$	Upper State energy / eV	Transition	A_{ki} / s^{-1}
H	410.2	13.2207	$n = 6 \rightarrow 2$	9.73×10^5
H	434.1	13.0545	$n = 5 \rightarrow 2$	2.53×10^6
H	486.1	12.7485	$n = 4 \rightarrow 2$	8.42×10^6
H	656.2	12.0875	$n = 3 \rightarrow 2$	4.41×10^7
H_2	600-630	13.8	$d \rightarrow a$	2.57×10^7

Figure 2.3 – Photograph of W substrate in the presence of a H/Ar plasma at $F(H_2) = 300$ sccm and $F(Ar) = 300$ sccm, with $d_{\text{sub}} = 32$ mm and $d_{\text{wire}} = 0.01$ ”, illustrated with a representation of z .

Figure 2.4 – Table of values for H and H_2 emissions where λ_{obs} is the observed wavelength, and A_{ki} is the Einstein A coefficient.

2.2.2 Cavity Ring Down Spectroscopy

For CRDS the side viewports were replaced with arms attached by flexible bellows, highlighted in figure 2.5. These side arms form the linear cavity through which the laser light travels, as described in section 1.5.2. At the end of the arms sit the precision adjustable mirror mounts, which contain high-reflectivity (99.5 %) mirrors. A separate $F(H_2)$ was introduced to the side arms to ensure a thorough distribution within the large reactor volume, and the $F(H_2)_{\text{total}}$ was taken as the sum of the central and side arm flows, $F(H_2)_{\text{cavity}}$ and $F(H_2)_{\text{arms}}$. The side arms were mounted to a separate platform than the main reactor, along with the photo-multiplier detector. This additional platform may be raised and lowered to alter the laser path through the chamber as a value of z , offering the full height of the plasma to probing. The value of $z = 0$ was taken as the height at which the substrate obstructs transmission of the laser.

The initial laser light is generated at 1063.2 nm by an Neodymium³⁺ doped yttrium aluminium garnet (NdYAG) laser and its λ is reduced to 354.4 nm by a frequency tripling crystal. This light then pumps a dye laser (Continuum Surelite III plus Spectra-Physics PDL-3) at 30 Hz, from which a series of beam steering and shaping optics direct the laser output into the reactor. 505.06 nm light from the dye laser is refracted by two prisms into a frequency doubling crystal

which halves the λ to 252.53 nm, necessary for probing the triplet transition of the Si atom. The beam is refracted and then narrowed by a series of pinholes and directed through a periscope of two 90° prisms to allow for the variable platform height. The top of the periscope is mounted on the adjustable platform, thus refracts the laser light through a long focal length lens into the linear cavity of the reactor. The light is reflected back and forth in the cavity, with a small minority of light transmitted through the exit mirror and collected using a photomultiplier tube to produce an output signal exhibiting the characteristic exponential decay.

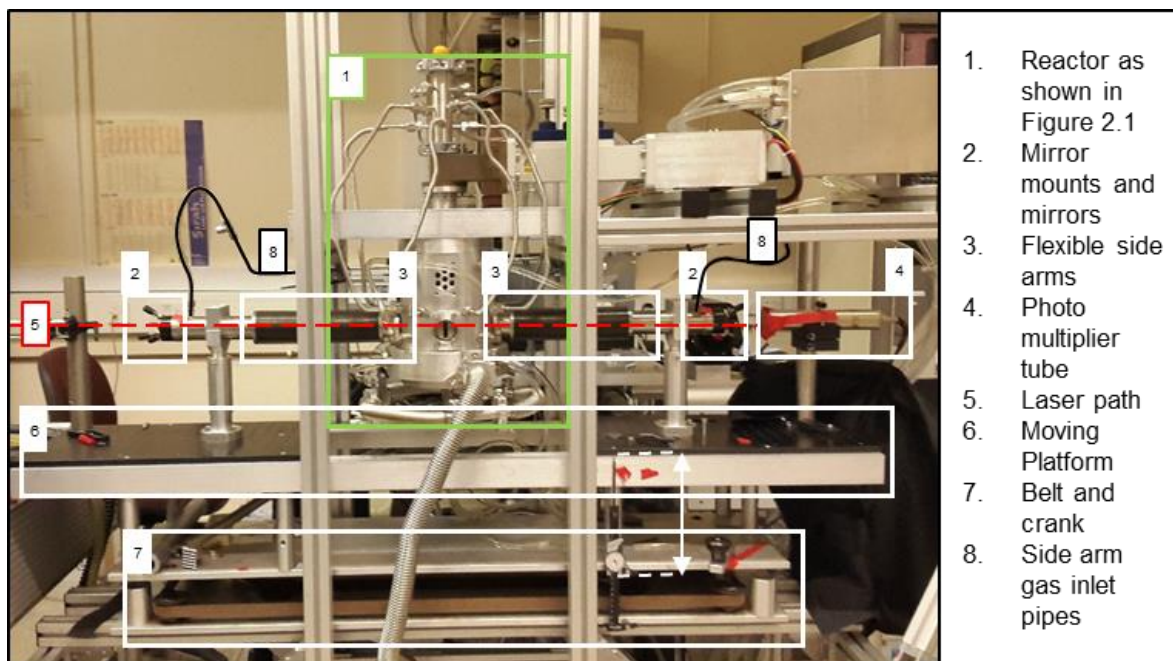


Figure 2.5 – Schematic overlay of the CRDS set up, illustrating the location of key components.

All the CRDS data was collected in the custom-written LABVIEW programs displayed in figures 2.6 and 2.8, communicating via a general purpose interface bus interface with an 8 bit digital oscilloscope (LeCroy 9361, dual channel, 300 MHz, 2.5 Gsamples/s).⁹ The output signal, visualised in figure 2.6 represents a) the intensity of transmitted light, I_t and its decay detected as a function of time, and b) the natural log of I_t against time. The gradient of the latter defines reciprocal of the ring-down lifetime, τ which varies with the absorbance. Consequently, scanning through λ from 251.3 to 251.5 nm, 252.3 to 252.5 nm, and 252.7 to 252.9 nm results in a peaked τ in the presence of Si. These correspond to absorption transitions from $3s^23p^2 \rightarrow 3s^23p4s$ for ground state of quantum number $J = 0$, $J = 1$ and $J = 2$ at 251.432 nm, 252.411 nm and 252.851 nm respectively, represented in figure 2.7.

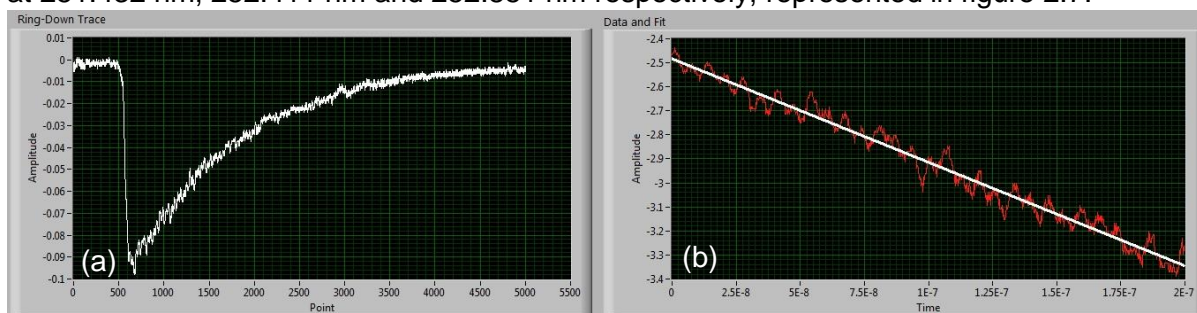
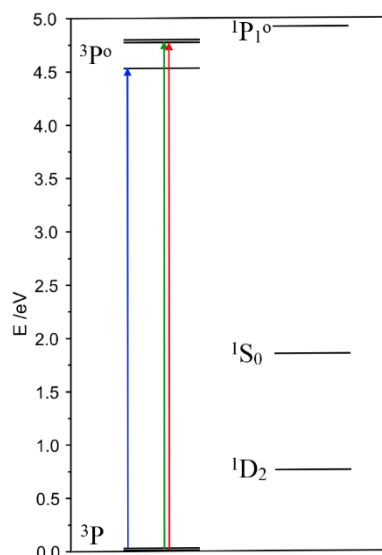


Figure 2.6 – The LABVIEW program display of a) ring-down trace, and b) the data and fit plot. The ring-down trace represents the real-time detection of I_t by the photomultiplier tube, and is defined by a vertical axis of light intensity and a horizontal axis of time. The ring-down data and line of best fit plot represents the natural log of the ring-down trace plotted on the vertical axis against time on the horizontal axis, with a line of best fit of resulting gradient equal to ring-down lifetime, τ .



λ_{absorb} /nm	Upper State energy / eV	g_i	Lower State energy / eV	g_k	Transition	A_{ki} / s ⁻¹
251.43	4.93	3	0	1	$^3P_1^o \leftarrow ^3P_0$	7.4×10^7
252.41	4.91	3	0.01	1	$^3P_1^o \leftarrow ^3P_0$	2.2×10^8
252.85	4.92	1	0.03	3	$^3P_0^o \leftarrow ^3P_1$	9.0×10^7

Figure 2.8 - Diagram showing singlet and triplet energy levels of the Si atom. The coloured arrows represent transitions that have been investigated via CRDS. These are the $J = 1 \leftarrow J = 0$ transition (red), $J = 0 \leftarrow J = 1$ transition (green), and Si $J = 1 \leftarrow J = 2$ transition (blue) as defined explicitly in the table of values where λ_{absorb} is the absorption wavelength, g_i and g_k are the upper and lower state degeneracies respectively and A_{ki} is the Einstein A coefficient.¹⁰

Upon driving through these absorption λ , three outputs are collected as a function of measurement count in the LABVIEW program; the ring-down time spectra, the mean squared error (MSE) and the etalon trace as displayed in figure 2.8. The ring-down time spectra is plot of $1/\tau$ against $1/\lambda$, which is wavenumber ($\bar{\nu}$). The ring-down time spectra is identifiable as a baseline with peaks, visible in figure 2.9a and present due to the change in ring-down time caused by an absorbing species as the dye laser λ grating is driven through its specific absorption peak. Each ring down time measurement has an associated MSE, this is the difference between the deviations of the ring-down data from line of best fit in figure 2.6b, and is similarly plotted in 2.9b. The MSE plot will show saturation, when ring-down decay becomes pulse-like and the MSE increases significantly. The MSE will also show slight increases at peak absorption. Figure 2.9c depicts the etalon trace, equally spaced sinusoidal fringes that fluctuate directly with change in λ . Due to the repeating nature of the etalon trace, we were able to assign a calibration scale using a $\bar{\nu}$ spectrometer and consequentially fit our absorption peaks to this scale.

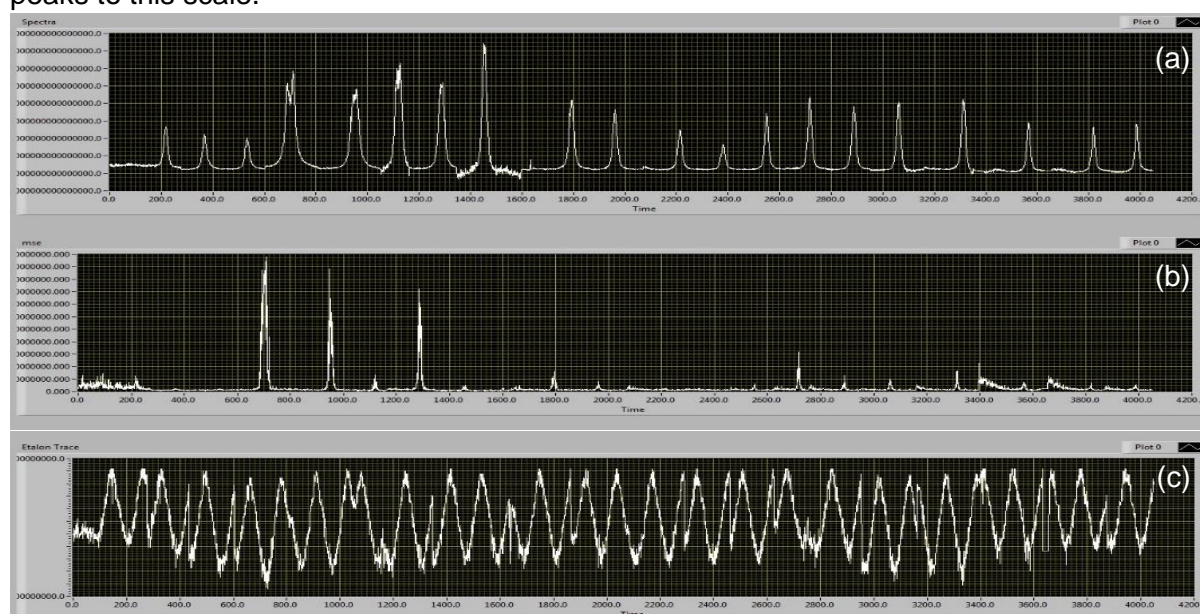


Figure 2.9 – The LABVIEW program display of the three outputs collected; (a) the ring down time spectra, a plot $1/\tau$ against $\bar{\nu}$, b) the MSE, calculated from the difference in the raw $1/\tau$ and the linear fit and plotted against $\bar{\nu}$, and c) the etalon trace, equally spaced sinusoidal fringes that fluctuate directly with change in λ , similarly plotted against $\bar{\nu}$.

From these three data plots, the value of interest is the Si column density, denoted at {Si} and calculated through equation 7:

$$\{Si\} = \frac{8\pi \times 10^{14} \times L}{A_{ki} \times \lambda^2} \times \frac{g_i}{g_k} \times \int \left(\frac{1}{\tau} - \frac{1}{\tau_0} \right) d\bar{\nu} \quad (7)$$

where the constants have been previously defined, barring τ_0 , the baseline ring-down lifetime and L, the length between the two mirrors (100 cm). Practically speaking, this represents an integration of the area under the absorption peaks in figure 2.9a, baselined against τ_0 .

2.3 References

1. M. N. R. Ashfold, E. J. D. Mahoney, S. Mushtaq, B. S. Truscott and Y. A. Mankelevich, *Chem. Commun.*, 2017, **53**, 10482-10495
2. A. Cheesman, J. A. Smith, M. N. R. Ashfold, N. Langford, S. Wright and G. Duxbury, *J. Phys. Chem. A*, 2006, **110**, 2821-2828
3. E. J. D. Mahoney, B. S. Truscott, S. Mushtaq, M.N.R. Ashfold and Y. A. Mankelevich, *J. Phys. Chem. A*, 2018, **122**, 8286-8300
4. E.J. D. Mahoney, S. Mushtaq, M. N. R. Ashfold and Y. A. Mankelevich, *J. Phys. Chem. A*, 2019, **123**, 2544-2558
5. E. J. D. Mahoney, B. S. Truscott, M. N. R. Ashfold and Y. A. Mankelevich, *J. Phys. Chem. A*, 2017, **121**, 2760-2772
6. J. Ma, M. N. R. Ashfold and Y. A. Mankelevich, *J. Appl. Phys.*, 2009, **105**, 43302-43312
7. NIST Atomic Spectra Database, https://physics.nist.gov/PhysRefData/ASD/lines_form.html, (accessed April 2019)
8. I. Banerjee, N. V. Kulkarni, S. Karmaker, V. L. Mathe, S. V. Bhoraskar and A. K. Das, *Plasma Sci. Technol.*, 2010, **12**, 27-30
9. J. Ma, J. C. Richley, M. N. R. Ashfold and Y. A. Mankelevich, *J. Appl. Phys.*, 2008, **104**, 103305-103309
10. E.J.D Mahoney, Unpublished PhD Thesis, University of Bristol, 2019

3. Results and Discussion

3.1 Optical Emission Spectroscopy of Hydrogen Plasmas

OES afforded an immediate spectrum, the raw data was captured by the CCD and visualised by the Andor Solis software, an example of which is given in figure 3.1a. The region of emission clearly defined in figure 3.1a highlights the height of the substrate, below the emission band as indicated, and the extent of the hot plasma region as defined by the emissions from the excited gas phase species detected. The vertical axis gives the height scale of the spectrum in pixels, and this was redefined as height above the substrate using the spatial calibration method outlined in section 2.2.1. The polynomial highlighted in the same section is required to regenerate the horizontal axis of figure 3.1a, defined by λ in nm, once the raw data has been run through MATLAB spatial calibration to generate a spectrum like those shown in figures 3.1b and 3.1c. Both figures illustrate the brightness of H_α emissions when compared to surrounding emissions like $H_2(d-a)$. A number of λ regions were observed using the diffraction gratings 1 and 2 specified in section 2.2.1, however figures 3.1 were captured using grating 1 centred at 600 nm, generating sufficient measurement to analyse the H_α and $H_2(d-a)$ emissions. It is noteworthy for later sections that H and H_2 emissions are sensitive to the hyperthermal component of the EEDF, and in order to probe the thermal component an alternative emitter must be used.¹

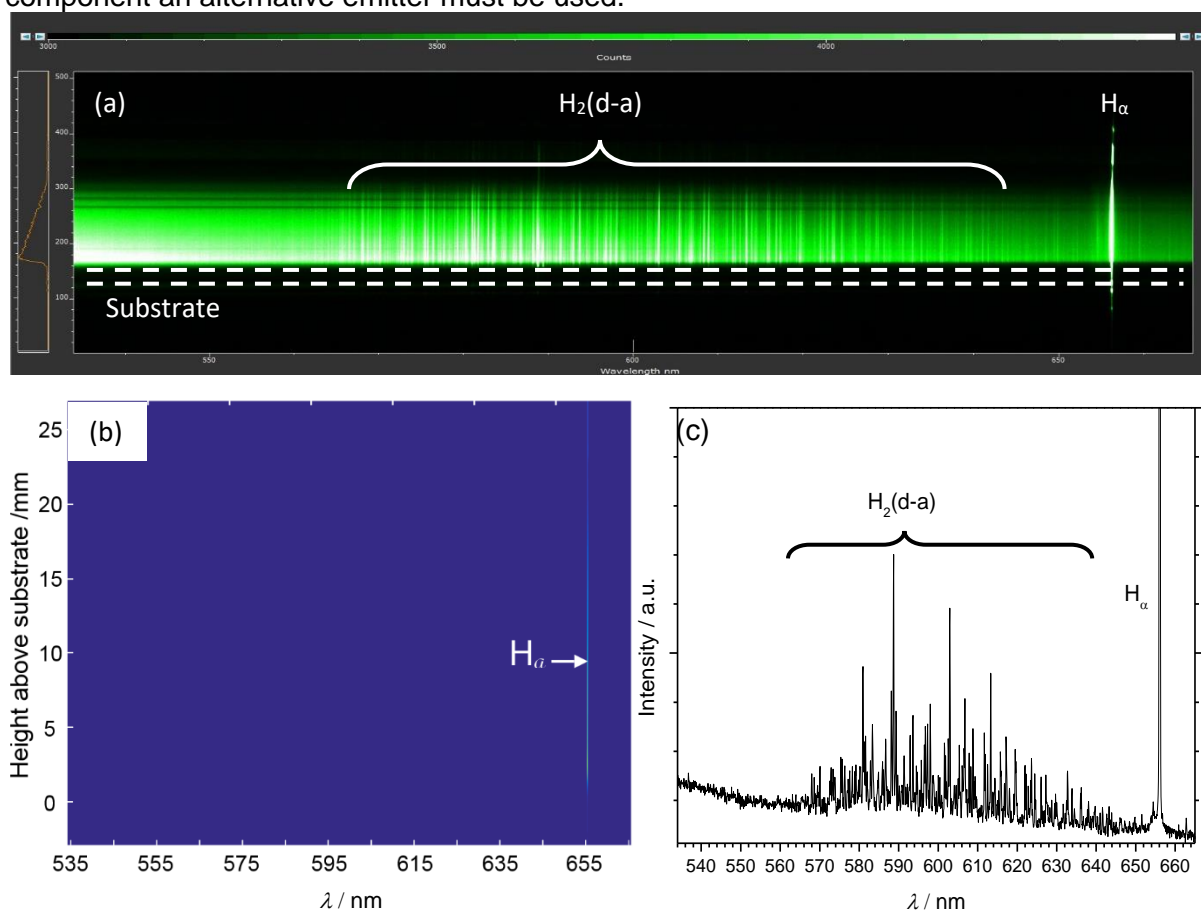


Figure 3.1a – OES Spectrum as visualised in Andor Solis Software, with horizontal scale of λ in nm and vertical scale of z in pixels, however the top of the green emission region lies at approximately $z = 20$ mm, and the dashed line indicates the substrate. This was collected with grating 1 at 600 nm (5 accumulations of 1.25 s exposure) of a solely H plasma at base conditions with a 32 mm W substrate.

Figure 3.1b – MATLAB generated 3D false colour plot of z against λ for the same emission range, highlighting the intensity of H_α relative to surrounding emissions.¹

Figure 3.1c – MATLAB generated 2D spectrum of I against λ for the same emissions in 3.1a and 3.1b, at single height above the substrate and reduced intensity.

For analysis of $H_2(d-a)$ emissions grating 2 was employed, centred over the 600 nm emission band shown in figure 3.1b. For each grating and λ range a spatial calibration is required (as summarised in section 2.2.1) to de-skew the vertical axis across the λ range, correcting for height above the substrate. From the MATLAB generated calibrated plot, spatial profiles at any z within the plasma may then be calculated from the relevant emission peaks.

3.2 Substrate Temperature Control

Spatial distributions were calculated from measurements of H_2^* and H^* emissions as a function of substrate temperature. Three variables were highlighted in sections 1 and 2 that significantly impact and offer a degree of control of T_{sub} , d_{wire} , d_{sub} and $F(Ar)$. T_{sub} has been suggested in literature to impact diamond growth, due to the significance of the gas phase and surface processes, notably affecting the migration of species across the substrate surface. Consequently, T_{sub} may also impact the emissions seen from excited species in the gas phase as discussed in section 1.3.^{1,2,3}

3.2.1 $H_2(d-a)$ and H_α as a function of Argon Flow Rate

The impact of Ar on MWPCVD was introduced in section 1.4.2, and presented the effects of Ar on the gas phase chemistry. It was noted that Ar rich plasmas impact the substrate heat transfer, resulting in higher T_{sub} at relatively increased $F(Ar)$. Ar emissions are detectable through OES, however it is the impact that Ar has on the plasma parameters, on H_α and $H_2(d-a)$ emissions and their respective emission intensities, $I(H_\alpha)$ and $I(H_2(d-a))$ that is of interest. These emissions were compared for $F(Ar)$ of 0 and 300 sccm, that is $X_0(Ar)$ of 0% and 50% as shown in figures 3.2 a and b respectively.

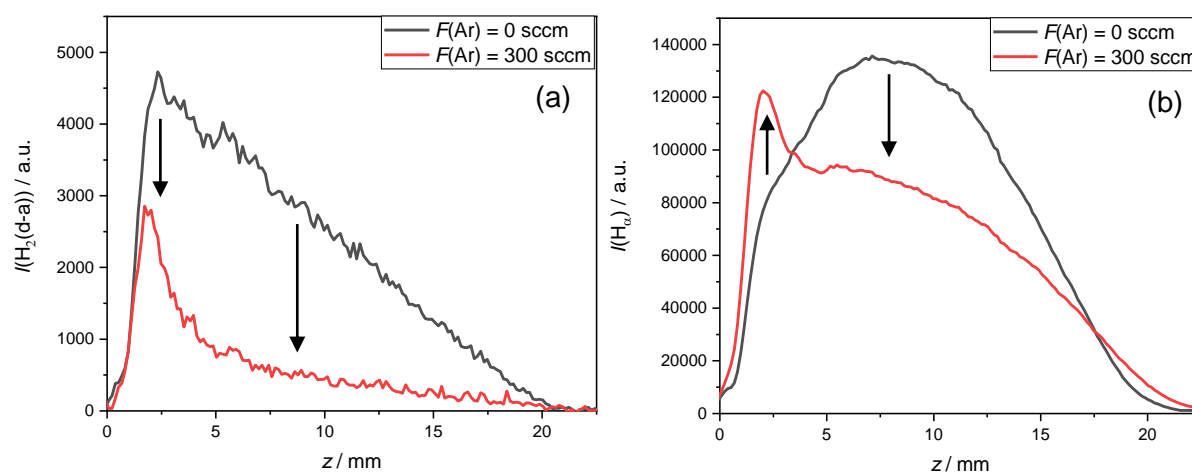


Figure 3.2 – a) $H_2(d-a)$ and b) H_α spatial as function of $F(Ar)$, W substrate $d_{sub} = 32\text{mm}$, $d_{wire} = 0.01''$.

The most notable effect of Ar on the emission intensities, is the relative increase in both $I(H_2(d-a))$ and $I(H_\alpha)$ close to the substrate compared to the full height of the plasma. In H_2 this is marked by a peak in intensity between 2 and 2.5 mm, but an apparent overall decrease in intensity from $F(Ar) = 0$ sccm to 300 sccm. For H_α , while the overall peak intensity appears to drop in intensity from approximately 3 mm, the initial $I(H_\alpha)$ close to the substrate surface is both maximum compared to the full emission with Ar present and a maximum at low z when compared to $F(Ar) = 0$ sccm. The introduction of Ar appears to reduce the overall emission intensities, but enhances the relative intensities at low z . We know that at $F(Ar) = 300$ sccm, $X_0(H_2)$ is halved and this is reflected in the large decrease in $I(H_2(d-a))$ in the centre of the plasma. The decrease in $I(H_2(d-a))$ is inhomogeneous however, with $I(H_2(d-a))$ showing a

relative increase at low z . From previous work, near resonant energy transfer is predicted to occur between Ar, H and H₂ excited and ground state species.¹ This is reflected in $I(\text{H}_2(\text{d-a}))$ maximising at low z , indicating an enhancement of the hyperthermal component of the EEDF. η_e is sufficiently diffuse that impact to the substrate surface will give the substrate a slight negative charge, consequently across the gap between the neutral plasma core, seen in figure 2.3, positive ions will accelerate towards the substrate resulting in ion bombardment and substrate heating. $|E|$ increases towards substrate, and although N also increases in a similar manner, $|E|/N$ can be suggested to correlate with $I(\text{H}_2(\text{d-a}))$ and maximise at low z by assuming η_e is generated by EIE alone. The EEDF will exhibit its highest energies where $|E|/N$ maximises, EIE will also increase in this region maximising the density of excited states, emission intensities, and also ionisation. $[\text{H}_2]$ is known from section 1.3.1, to maximise at high z near input gas inlets, but $I(\text{H}_2(\text{d-a}))$ is not seen in this region. We can therefore assume hyperthermal η_e does not extend significantly above $z = 20$ mm. The observations in $I(\text{H}_\alpha)$ can also be explained based on the near resonant energy transfer at low z , as Ar* is shown to maximise at the cooler, lower z regions. The decrease in $I(\text{H}_\alpha)$ seen at higher z , is compensated by production of H in the plasma core due to the reduced thermal conductivity from the introduction of Ar acting to increase thermal dissociation.

For $F(\text{Ar}) = 300$ sccm, T_{sub} was recorded as 995 °C using a two colour pyrometer, whereas a reading of approximately 700 °C was achieved from a one colour pyrometer at $F(\text{Ar}) = 0$ sccm. This rise in T_{sub} shown upon the introduction of Ar is likely a result of the subsequent reduced thermal conductivity. At higher T_{sub} , there is the potential for the substrate thermal energy to be partitioned to a greater degree by ion bombardment.

3.2.1 $\text{H}_2(\text{d-a})$ and H_α as a function of Substrate Diameter

As an alternative method of affecting T_{sub} ; the role of d_{sub} on $\text{H}_2(\text{d-a})$ and H_α emission profiles was investigated using W substrates with a d_{sub} of 17 mm and 32 mm, and a Mo coil wire of $d_{\text{wire}} = 0.01$ ". The data used to produce the spatial profile for $F(\text{Ar}) = 0$ sccm in figure 3.2 is that same as the data used for $d_{\text{sub}} = 32$ mm in figure 3.3 below.

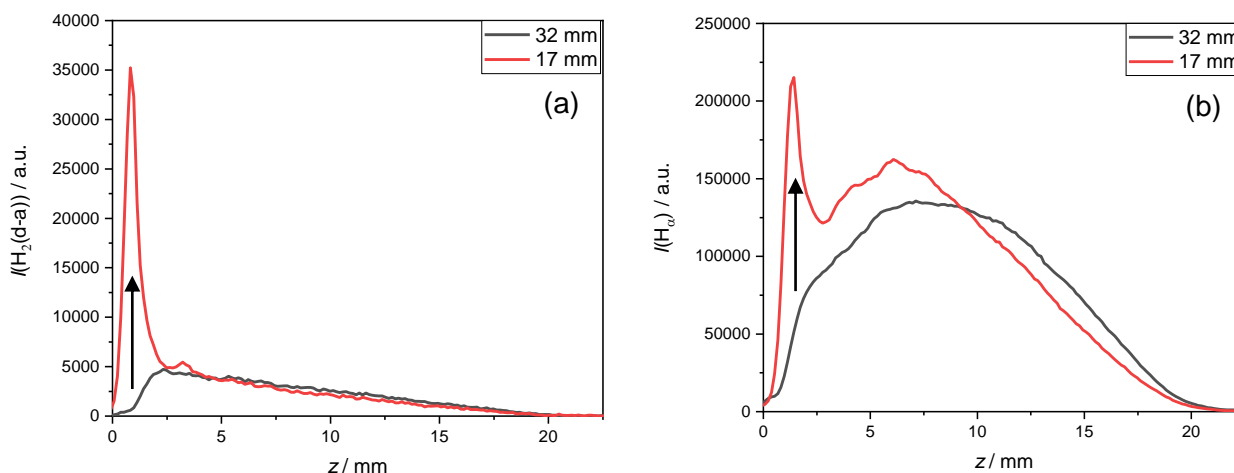


Figure 3.3 – a) $\text{H}_2(\text{d-a})$ and b) H_α spatial as function of d_{sub} , where $d_{\text{wire}} = 0.01$ ".

The variation in both $I(\text{H}_2(\text{d-a}))$ and $I(\text{H}_\alpha)$ across the height of the plasma for $d_{\text{sub}} = 17$ mm is comparable with the spatial profiles seen with $F(\text{Ar}) = 300$ sccm, however with some marked differences. Firstly, the overall intensity of both emissions is notably higher than both $F(\text{Ar}) = 300$ sccm and base conditions ($F(\text{Ar}) = 0$ sccm or $d_{\text{sub}} = 32$ mm). For $\text{H}_2(\text{d-a})$ this is evident in a dramatically higher peak $I(\text{H}_2(\text{d-a}))$ at approximately 1 mm, and a comparable $I(\text{H}_2(\text{d-a}))$ at

higher z . This represents an increase in the hyperthermal component with decreasing d_{sub} . For $I(H_\alpha)$ with $d_{sub} = 17$ mm and $d_{wire} = 0.01''$, the profile appears bimodal with a primary peak close to the substrate surface, this peak is higher than the secondary broad peak, which is also higher and closer to the substrate than the single broad peak shown at base conditions.

Decreasing d_{sub} appears to increase t_{sub} . This was evident in both $I(H_\alpha)$ and $I(H_2(d-a))$, which peaked at low z , approximately 2 mm above the substrate when $d_{sub} = 17$ mm. Once again both $I(H_\alpha)$ and $I(H_2(d-a))$ are maximising with $|E|/N$ at low z , close to the substrate surface. Using the smaller d_{sub} , there is this observed enhancement of the $|E|/N$ evidenced by the increased $I(H_\alpha)$ and $I(H_2(d-a))$ at low z , and consequently the enhancement of the hyperthermal component of the EEDF. η_e is maximising at the edge of the substrate, however as OES measurements are not localised but linear through the plasma, emission intensities will be detected as an amalgamation across the whole plasma. H_3^+ will also maximise close to the substrate, increasing ion bombardment. The higher η_e is speculated to be originating to some extent from thermionic emission and an increase in secondary electrons emitted from the surface.

For $d_{wire} = 0.01''$ and $d_{sub} = 32$ mm, T_{sub} was less than 700°C, whereas for $d_{sub} = 17$ mm, T_{sub} was recorded as approximately 1150 °C, and the observed increase in both $I(H_2(d-a))$ and $I(H_\alpha)$ close to the substrate relative to the total emission is indicative of this higher T_{sub} .

3.2.1 $H_2(d-a)$ and H_α as a function of Wire Spacer Diameter

The third method for changing T_{sub} was introducing a coil wire of varying d_{wire} between the substrate and the base plate, notably the 17 mm substrate as the impact of d_{wire} was not seen with the 32 mm substrate. As introduced in section 1.3 and discussed further in section 2.1.2, the diameter of a coil wire, d_{wire} alters the volume of the gas gap between the substrate and the copper base plate, thus impacting the degree of conductive cooling. As with $F(Ar)$ and d_{sub} , d_{wire} was varied and the resulting $H_2(d-a)$ and H_α emission profiles captured with OES. The values of $d_{wire} = 0''$, 0.004'', 0.008'' and 0.01'' for a Mo coil wire on a 17 mm W substrate were investigated at base conditions.

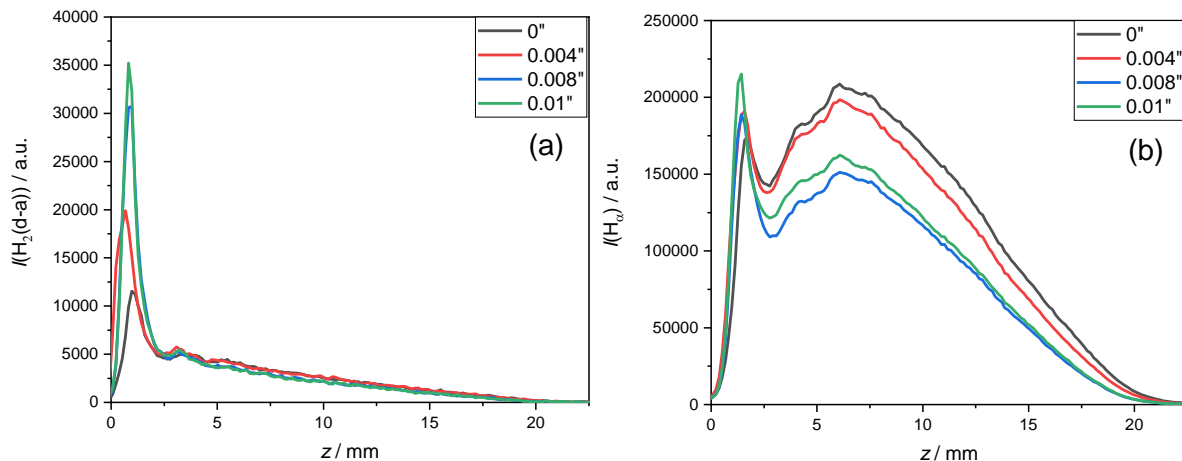


Figure 3.4 – a) $H_2(d-a)$ and b) H_α spatial as function of d_{wire} , where $d_{sub} = 17$ mm.

On initial inspection both $I(H_\alpha)$ and $I(H_2(d-a))$ plainly demonstrate an enhancement at low z with increasing d_{wire} , when using a reduced d_{sub} . The centre of the plasma appears less affected by changes in d_{wire} , only through variations in the overall emission intensity. Similarly to d_{sub} , d_{wire} variation acts to increase the absolute intensities of these emissions at low z , by enhancing the hyperthermal component of the EEDF at these heights. Above approximately

3 mm $I(\text{H}_2(\text{d-a}))$ shows little disparity with d_{wire} , whereas $I(\text{H}_\alpha)$ shows a significant degree of variation. The lower values of d_{wire} appear to contribute to a higher $I(\text{H}_\alpha)$ above 3 mm, excepting $d_{\text{wire}} = 0.008''$, which shows a smaller secondary peak than expected with this trend. It is important to note that the H_α profiles also vary in the order the measurements were carried out. This could suggest that the variation arising from the deposition chamber opening and closing between alterations of d_{wire} , may be impacting the overall value of $I(\text{H}_\alpha)$. If this is the case, $I(\text{H}_\alpha)$ appears to be far more sensitive than $I(\text{H}_2(\text{d-a}))$ to such variations as both emissions were captured in the same plasma for each value of d_{wire} . The emissions were normalised to the various shared profile features in figures 3.5 to investigate these abnormalities. Upon normalisation, it can be seen that the H_α emission profile for $d_{\text{wire}} = 0.008''$ does fit with the trends; its primary peak lying above $d_{\text{wire}} = 0.004''$ and below $0.01''$ and its secondary peak remaining below $d_{\text{wire}} = 0.004''$, but above $0.01''$.

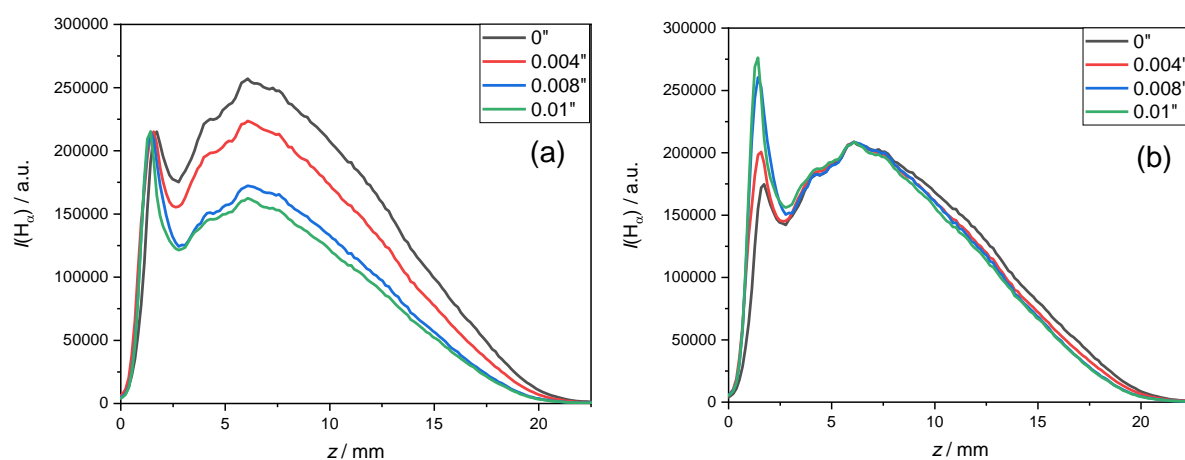


Figure 3.5 – H_α spatial profiles as function of d_{wire} , normalised to the a) primary and b) secondary peak heights.

For figure 3.4, two-colour pyrometer measurements were as follows: $d_{\text{wire}} = 0.004''$ $T_{\text{sub}} \approx 700$ °C, $d_{\text{wire}} = 0.008''$ $T_{\text{sub}} \approx 1100$ °C, and $d_{\text{wire}} = 0.01''$ $T_{\text{sub}} \approx 1150$ °C. At $d_{\text{wire}} = 0''$, T_{sub} was below the lower limit (700 °C) of the pyrometer. The increased gas gap brought about by increasing d_{wire} , reduces the rate of conductive heat transfer from substrate to the reactor baseplate, resulting in an increasing t_{sub} . At $d_{\text{wire}} = 0''$, the gas gap is essentially non-existent and conductive heat transfer is most efficient. The flux of conductive heating from the gas phase is effectively constant with varying d_{wire} , and only the rate of energy loss from the substrate is changing. The energy partitioned through thermionic emission will therefore increase, as the rate of conductive heat transfer decreases. This may result in an increase in η_e near the substrate surface, the additional η_e originating to some extent from an increase in thermionic emission and secondary electrons emitted from the surface.

Both $\text{H}_2(\text{d-a})$ and H_α emissions have been shown to vary with T_{sub} , and d_{wire} . Had it been practical, all three variables used to impact T_{sub} may have been varied further, potentially offering insight into their respective effectivity as influencers of T_{sub} . The results gathered showed an association with the hyperthermal EEDF, and indicated a sensitivity of the EEDF to T_{sub} , and subsequently d_{wire} , however it is possible variations in T_{sub} and the spatial profiles may arise from different manifestations of the physical and chemical processes. T_{sub} may be more closely related to the thermionic emission, or a manifestation of decreased thermal conductivity and enhanced ion impact ionisation.

As well as impacting emissions from excited state species, T_{sub} will impact the degree of etching from the substrate surface. This is noteworthy in the use of Si substrates or for purposeful etching of metals into the gas phase, the latter coming into consideration in the following investigation. In section 1.5.1 it was briefly mentioned OES may be used to probe the EEDFs of MWPCVD plasmas in order to estimate the associated T_e . The nature of both $H_2(d-a)$ and H_α offer a probe of the hyperthermal component of the EEDF, and these have been used to demonstrate changes in $I(H_2(d-a))$ and $I(H_\alpha)$ for varying d_{wire} . In order to investigate the thermal component an alternative emitter must be used.

3.3 Probing Electron Temperature through Aluminium Emissions

3.3.1 Aluminium Substrate

In section 1.6 the concept of etching metals, notably Al into the gas phase was addressed. Al has been shown to exist in the gas phase as excited state species when an Al target is subject to suitable conditions, and much like Si it is believed Al gas phase will be generated through plasma etching.^{4,5} Previous OES on the H Balmer series has used the emission intensity ratio between H emissions to estimate electron temperature, however this method only probes the hyperthermal component of the EEDF.⁶ Al is perhaps an alternative emitter that may offer a probe of the thermal component of the EEDF. Al has a range of energy levels which might couple the thermal component and consequently numerous Al emissions are quoted in literature, correlating to high Einstein A coefficients. Most notably in a H plasma in the presence of an Al substrate as defined in section 2.1.2., the Al I lines seen at 308.22 nm, 309.27 nm, 394.40 nm and 396.15 nm, henceforth referred to as Al(1), Al(2), Al(3) and Al(4) respectively, which are detected as sharply resolved peaks, within the range of the H Balmer series.^{4,5,7} This is illustrated in spectra in figure 3.7.

The λ range in figure 3.7 captures the Al I emissions Al (3) and Al(4), due to the $3s^24s \rightarrow 3s^23p$ transition, as well as H_δ at 410.17 nm and H_γ at 434.04 nm. However, although promising, achieving these emissions required significantly irregular plasma conditions.⁴ At low T_{sub} ($d_{wire} = 0''$, $d_{sub} = 32$ mm, plasma base conditions), emissions were relatively weak and poorly resolved, as such no Al spatial profiles have been calculated. Upon raising T_{sub} ($d_{wire} = 0.004''$) emissions were resolved, however upon increasing P to base conditions the plasma was unstable, and flickered. It is noted that the melting point of Al is approximately 660 °C.⁸ Although T_{sub} for this d_{wire} fell below the pyrometer lower limit of 700 °C, the Al substrate itself was evidently hot, evidenced by the bright red emissions and Al clusters that were seen to eject from the substrate surface as visible trails, assumedly from thermal decomposition. It is also noted that AlH emissions were seen under significantly energetic conditions.⁹ Upon removal of the substrate from the deposition chamber it was noted that the Al and W substrates appeared tarnished, with the Al substrate outline left on the surface of the W substrate. This could suggest the substrate was close to its melting point. The emissions seen in figure 3.7 were achieved at 1.4 kW and 202 Torr, at which point the plasma demonstrated instability and flickering, and subsequently the Al substrate was replaced with an Al_2O_3 substrate. Al_2O_3 has a significantly higher melting point at 2072 °C will offer a more stable substrate with a more controlled introduction of Al to the gas phase.¹⁰

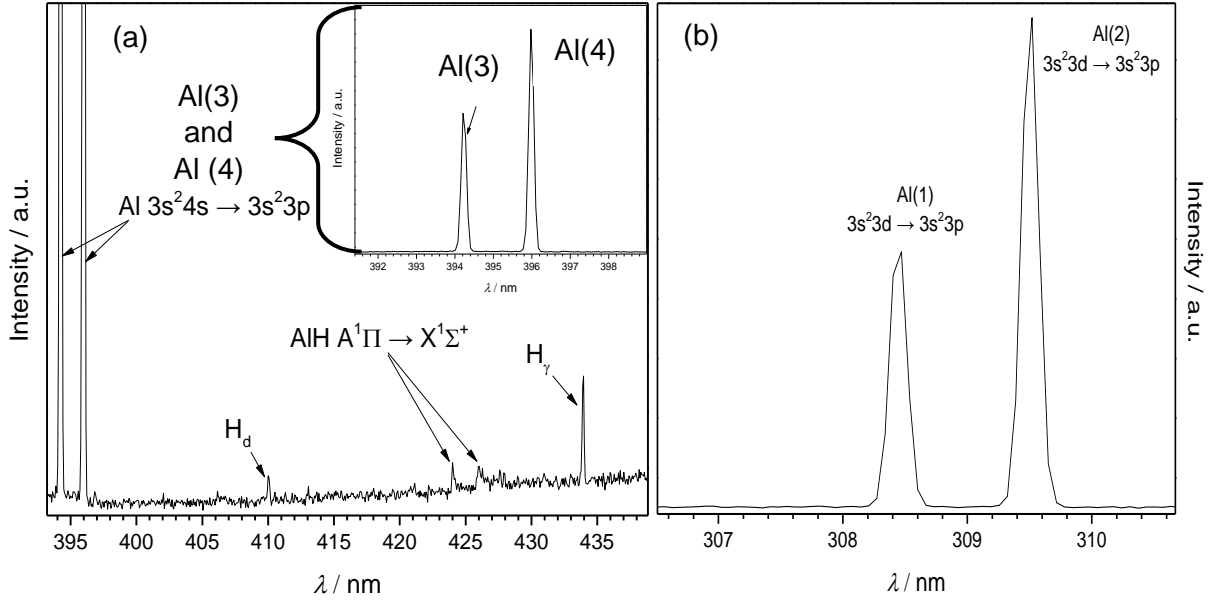


Figure 3.7 – a) Emissions detected at a single height for H plasma at 1.4 kW and 202 Torr, with an Al substrate on a 32 mm W substrate, $d_{wire} = 0.004''$. The inset shows Al(4) and Al(3) at a different scale to highlight the emission intensity ratio. b) As with Al(4) and Al(3), at a suitable scale Al(2) and Al(1) visibly demonstrate a 2:1 ratio as a doublet arising from the same energy state transition.

3.3.2 Aluminium Oxide Substrate

For the remainder of the investigation into Al emissions, an Al_2O_3 substrate, as defined in section 2.1.2 was used to generate Al species in the gas phase. As with the Al substrate, emissions from Al I excited states were detected through OES, however with the Al_2O_3 substrate these were resolved at the full range of plasma conditions. Figures 3.8 illustrates the emissions detected at base conditions for a H plasma in the presence of an Al_2O_3 substrate. In figure 3.8b all four prominent Al emissions; Al (1) and Al(2), and Al(3) and Al(4) due to $3s^23d \rightarrow 3s^23p$ and $3s^24s \rightarrow 3s^23p$ transitions respectively can be seen, with second order duplicates of the same transitions seen at higher λ in figure 3.8b.⁷ Al(1-4) were identified as suitable candidates for probing the thermal component of the EEDF due to their energy state levels and strong emission intensities, assuming these states are generated by EIE of the Al ground state. Under this assumption, $I(Al)$ can be described by equation 8:¹¹

$$I(Al) = \frac{\varepsilon g_i A_{ki} \eta(E) k_{EIE}[Al]}{\lambda (k_Q[Q] + A_{ki})} \quad (8)$$

where ε is the detection efficiency of the optical system at relevant λ , $k_Q[Q]$ is the rate of quenching, k_{EIE} is the rate of EIE, $\eta(E)$ is the η_e at the emission energy E and all other terms have been previously defined. These four emissions appear as two pairs of doublet emissions corresponding to the two electronic transitions noted and differing within the pairs of Al(1) and Al(2), and Al(3) and Al(4) by the J quantum number of their lower and upper electronic levels respectively. When compared to their partner, the longer emission appears to be double the intensity of the shorter emission, as highlighted in figure 3.7c. The ratios of two emitting states can be related by equation 9:

$$\frac{I(Al(2))}{I(Al(1))} = \frac{g_{Al(2)} \eta(E)_{Al(2)} \lambda_{Al(1)} A_{Al(2)} k_{Al(2)}[Q] \varepsilon_{Al(2)}}{g_{Al(1)} \eta(E)_{Al(1)} \lambda_{Al(2)} A_{Al(1)} k_{Al(1)}[Q] \varepsilon_{Al(1)}} \quad (9)$$

where the emission intensity ratio of Al(2) and Al(1) is used. As they arise from the same transitions, by assuming $k_Q[Q]$ to be one, with both states quenching at the same rate and

using an ε of approximately 3.5 estimated from previous data, equation 9 can be simplified to equation 10:

$$\frac{I(Al(2))}{I(Al(1))} = \frac{g_{Al(2)} A_{Al(2)}}{g_{Al(1)} A_{Al(1)}} \quad (10)$$

Using the values in figure 3.8c, doublets demonstrate a 2:1 ratio because of the relative ratios of their A_{ki} and g_i . The emissions were seen experimentally to maintain this ratio, irrespective of process conditions. Thus when estimating T_e using a Boltzmann distribution, the emission intensity ratio of Al(1) and Al(4) was used, as they arise from different upper states. In this circumstance, the assumptions underpinning equation 10 would longer be appropriate. The ratio of $\eta(E)$ can be related to $k_B T_e$ through the boltzman distribution, described in equation 11:¹¹

$$\frac{\eta(E)_{Al(4)}}{\eta(E)_{Al(1)}} \propto \frac{g_{Al(4)}}{g_{Al(1)}} e^{\frac{-\Delta E}{k_B T_e}} \quad (11)$$

where ΔE is the energy difference between the upper states and k_B is the Boltzmann constant.

(a)	$\lambda_{obs} / \text{nm}$	Upper State energy / eV	g_i	Lower State energy / eV	g_k	Transition	A_{ki} / s^{-1}
	256.9	4.8266	4	0.000	2	$3s^2nd ({}^2D, {}^3/2) \rightarrow 3s^23p ({}^2p^0, {}^1/2)$	1.92×10^7
	257.7	4.8272	6	0.014	4	$3s^2nd ({}^2D, {}^5/2) \rightarrow 3s^23p ({}^2p^0, {}^3/2)$	3.60×10^7
	257.7	4.8266	4	0.014	4	$3s^2nd ({}^2D, {}^3/2) \rightarrow 3s^23p ({}^2p^0, {}^3/2)$	5.99×10^6
	265.5	4.6729	2	0.000	2	$3s^25s ({}^2S, {}^1/2) \rightarrow 3s^23p ({}^2p^0, {}^1/2)$	1.42×10^7
	266.2	4.6729	2	0.014	4	$3s^25s ({}^2S, {}^1/2) \rightarrow 3s^23p ({}^2p^0, {}^3/2)$	2.84×10^7
Al(1)	308.4	4.0215	4	0.000	2	$3s^23d ({}^2D, {}^3/2) \rightarrow 3s^23p ({}^2p^0, {}^1/2)$	5.87×10^7
Al(2)	309.5	4.0217	6	0.014	4	$3s^23d ({}^2D, {}^5/2) \rightarrow 3s^23p ({}^2p^0, {}^3/2)$	7.29×10^7
	309.5	4.0215	4	0.014	4	$3s^23d ({}^2D, {}^3/2) \rightarrow 3s^23p ({}^2p^0, {}^3/2)$	1.16×10^7
Al(3)	394.4	3.1427	2	0.000	2	$3s^24s ({}^2s, {}^1/2) \rightarrow 3s^23p ({}^2p^0, {}^1/2)$	4.99×10^7
Al(4)	396.1	3.1427	2	0.014	4	$3s^24s ({}^2s, {}^1/2) \rightarrow 3s^23p ({}^2p^0, {}^3/2)$	9.85×10^7

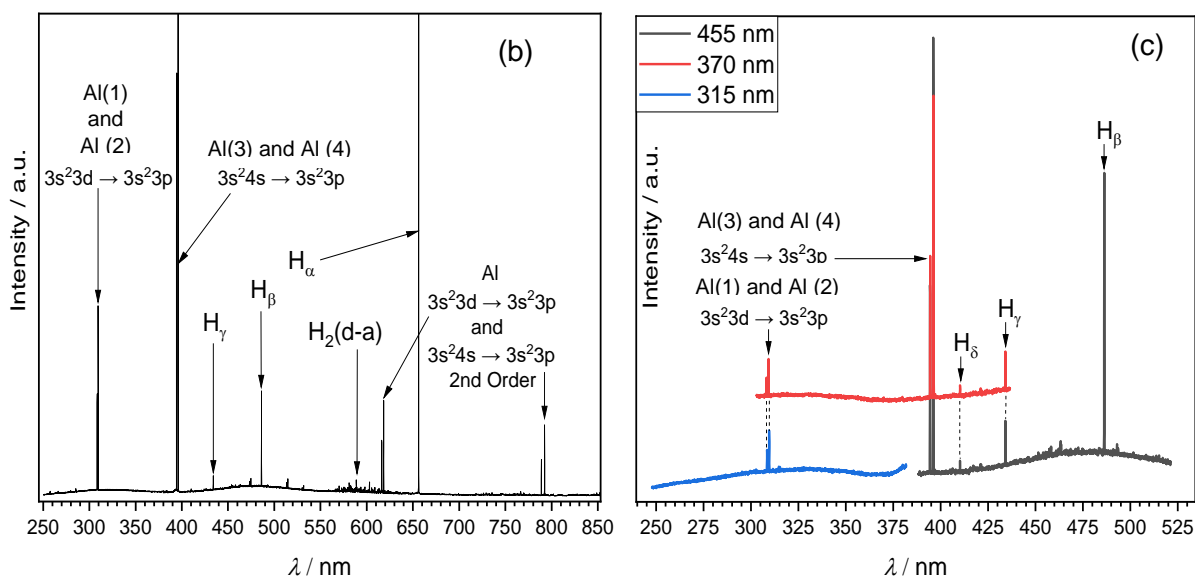


Figure 3.8 – a) Emission line plot identifying prominent emissions defined explicitly in c) a table of values relevant to the Al emissions observed, where λ_{absorb} is the absorption wavelength, g_i and g_k are the upper and lower state degeneracies respectively and A_{ki} is the Einstein A coefficient.⁷ The emissions were detected at single height at multiple OES λ ranges for an Al_2O_3 substrate placed centrally on a 32 mm W substrate, under a H plasma at base conditions, $d_{wire} = 0.01''$ b) Emission line plot identifying prominent emissions detected at low z under the same conditions within the three OES λ ranges selected.

The H Balmer series is also clearly observed, although H_α and H_σ are only identified in figure 3.8a and 3.8b respectively. The three λ ranges shown in figure 3.8b illustrate the use of grating 1, centred at 315 nm, 370 nm and 455 nm to generate an overlapping emission spectrum that captured all four prominent Al emissions and a significant number of H emissions. In a similar manner figure 3.8a was generated from 5 separate λ ranges. At base conditions spatial profiles for all of the 7 emissions captured by the three λ ranges were calculated and a selection are compiled in figures 3.9. The first assessment of Al(1), Al(2), Al(3) and Al(4) in figure 3.9a demonstrates that when normalised to the same peak intensity, all four emissions captured in the 370 nm range demonstrated a comparable spatial profile. A maximum $I(\text{Al})$ is detected at approximately 2 mm, as seen with both $H_2(\text{d-a})$ and H_α and then the Al emission falls to near zero by 7.5 mm above the substrate surface. This localisation to low z , highlights a flaw with the method of introducing Al to the gas phase. It is noted that the Al_2O_3 substrate lies on top of the W substrate so may alter the value of $z = 0$ and that Al(3) and Al(4) highlight an unsteady decrease in $I(\text{Al})$ around 3 mm in figure 3.9d, possibly arising from a bimodal edge effect of the plume emission (see figure 2.2) if $|E|$ is larger, however it was not time permitting to investigate these abnormalities further.

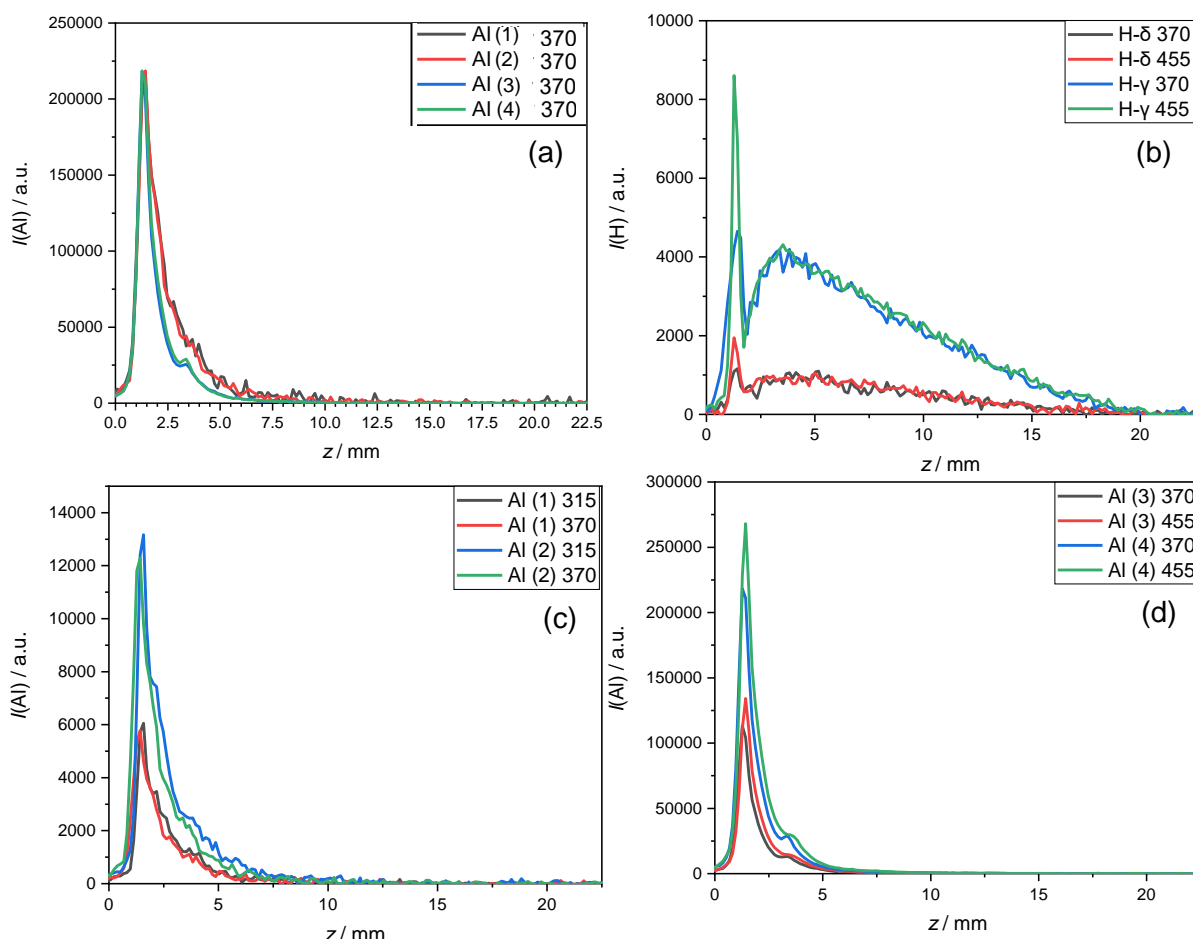


Figure 3.9 –Spatial profiles calculated at base conditions, with no wire spacer for a) the four Al emissions for grating 1 centred at 370 nm, b) H_δ and H_γ for grating 1 centred at 370 nm and 455 nm, c) Al(1) and Al(2) for grating 1 centred at 315 nm and 370 nm, and d) Al(3) and Al(4) for grating 1 centred at 370 nm and 455 nm.

After assessing all four Al peaks together, the emissions were compared between the three λ ranges in figures 3.9b, c and d. In figure 3.9b initial assessment of H_δ and H_γ showed a high degree of correlation between λ ranges 370 nm and 455 nm, barring a significant disparity between primary peak intensities. This may likely be attributed to the degree of resolution at

these lower intensity emissions or the emission λ as a function of the angle of the diffraction grating. It is clear however from figure 3.9b, that H_γ is of a higher intensity and resolution than H_δ , and not shown here but brighter still yet still correlating is H_β . For this reason H_β captured in λ range 455 nm was used for the remainder of the Al investigation due to its higher intensity and resolution. In figures 3.9c and d a similar overlay highlighted the comparability for calculated spatial profiles of Al emissions, with a notable minor variation in peak intensity between λ ranges. For practical reasons further spatial analysis of Al emissions were carried out at grating 1 centred at 370 nm, as all four emissions were captured within this λ range.

OES measurements were captured for an Al_2O_3 substrate under a range of process conditions; d_{wire} , $F(\text{Ar})$, p and P . Spatial profiles for the H_β emission captured in grating 1 centred at 455 nm were calculated for the range of conditions and the calculated spatial profiles for H_β are displayed in Figure 3.10. Some agreement is shown with the H_α emissions variation in section 3.2.1; the H_β emissions show a primary peak, at low z close to the substrate surface where the hyperthermal component of the EEDF is enhanced. The secondary peak at approximately 4 mm, then $I(H_\beta)$ falls slowly towards $z = 20$ mm. Once again, as with H_α the secondary peak height decreases with increasing value of d_{wire} in figure 3.10a, but it is important to note these conditions were measured across a number of plasmas and the variation from opening and closing the deposition chamber has been previously demonstrated in figure 3.4b to have an impact.

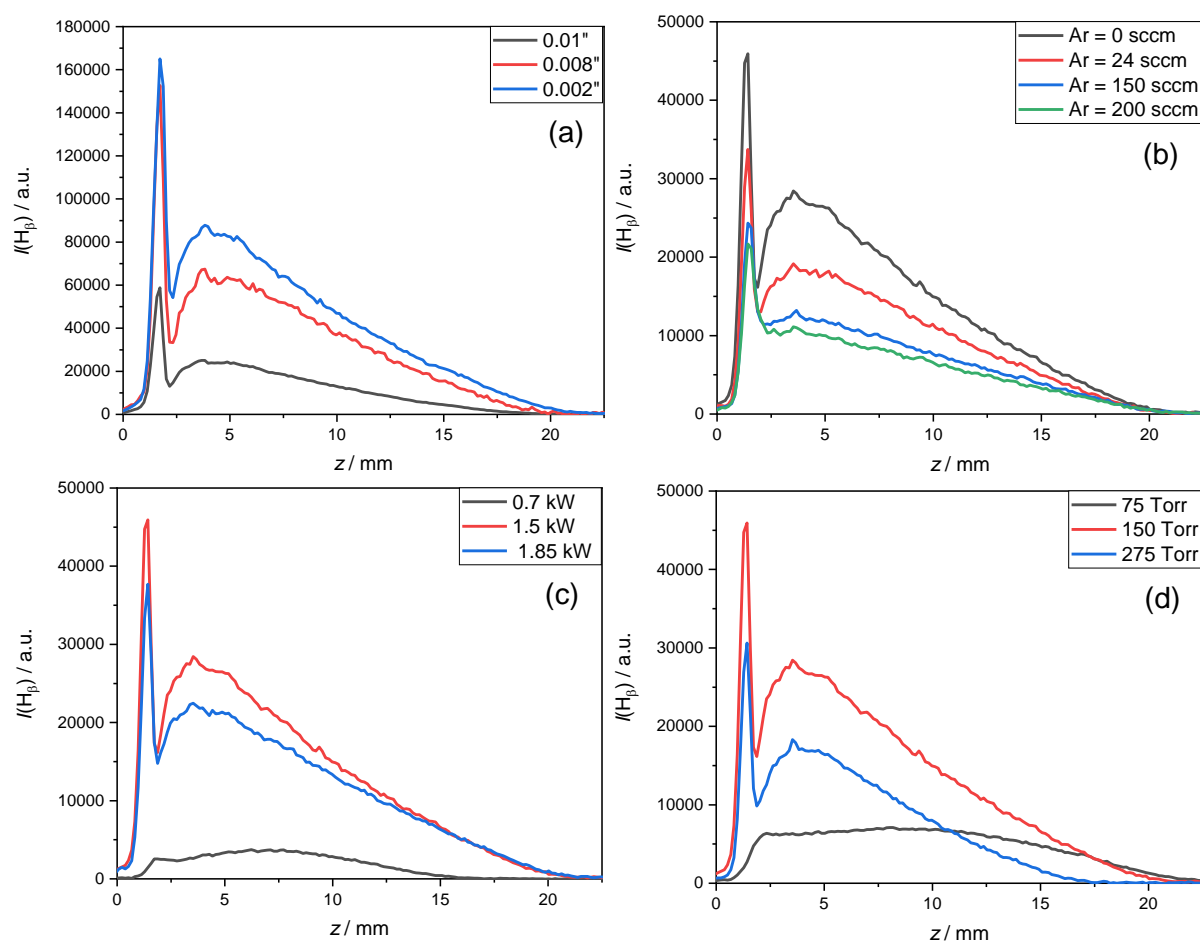
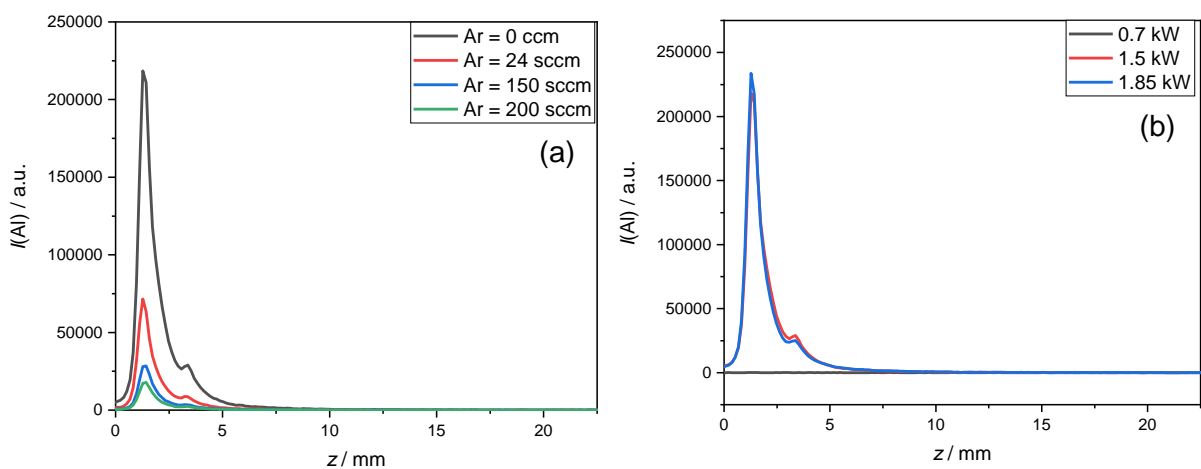


Figure 3.10 – Spatial profiles calculated a) H_β as a function of d_{wire} at base conditions, b) H_β as a function of $F(\text{Ar})$ at base $F(\text{H}_2)$, p and P , c) H_β as a function of P at base $F(\text{H}_2)$ and p , and d) H_β as a function of p at base $F(\text{H}_2)$ and P for an Al_2O_3 substrate on a W substrate with $d_{\text{sub}} = 32$ mm, and for b), c) and d) $d_{\text{wire}} = 0.002$ ".

In figure 3.10a the notable difference is in the primary peak, unlike in the H_α emissions, the overall $I(H_\beta)$ appears to decrease with increasing d_{wire} . Figure 3.10b illustrates the variation of $I(H_\beta)$ with $F(Ar)$, showing an decrease in the overall emission intensity as $F(Ar)$ is increased. Figure 3.10 c and d suggests a non-linear relationship between $I(H_\beta)$ and MW P , $I(H_\beta)$ is observed at higher z values with increasing P due to the increase in plasma volume that occurs to maintain P density. $I(H_\beta)$ varies in a similar manner as a function of p in figure 3.10d, however accompanied by a decrease of $I(H_\beta)$ at higher z values due to plasma contraction. For both P and p the primary peak and secondary peaks appear at base conditions, however though these features persist, $I(H_\beta)$ appears to fall again at the higher condition parameters.

Increasing d_{wire} with an Al_2O_3 substrate present acted to decrease $I(H_\beta)$. This can be attributed to an increase in the T_{sub} , acting to enhance gas phase $[Al]$. When compared to H or H_2 , Al has a significantly lower ionization energy, therefore would increase η_e and decrease the hyperthermal component, justifying the reduced $I(H_\beta)$ with increasing d_{wire} . For $I(H_\beta)$ as a function of $F(Ar)$, the overall $I(H_\beta)$ decreases with increasing $F(Ar)$. This somewhat contrasts the variation seen with H_α , where the low z $I(H_\beta)$ appeared more prominent with increased $F(Ar)$, but this might be a manifestation of the different d_{wire} or Ar acting to quench Al as the prominent cation. The increase in $I(H_\beta)$ seen when increasing both P and p to base conditions can be attributed to a shift in the prominent cation from H_3^+ to Al^+ , shown by the emergence in $I(Al)$ in figures 3.11. Upon increasing these parameters above base conditions, an increase in $[Al]$, will result in a suppression of the hyperthermal component of the EEDF, as with d_{wire} accounting for the decrease in $I(H_\beta)$. On comparison between studies with and without an Al_2O_3 substrate present, H Balmer emissions demonstrate notably different trends when varying the common parameter, and these indicate significant changes to the hyper-thermal component of the EEDF when Al is present. It suggests the spatial distribution variations are in some extent related to substantial local changes in the I^E/N from the presence of the small Al_2O_3 substrate.

Spatial profiles were also calculated under the same plasma conditions for Al emissions, barring d_{wire} where different λ ranges were used between changes in d_{wire} . This should also be noted as a potential increase in the error for figure 3.10a. Figures 3.11a, b and c show the behaviour of $I(Al)$ in response to changes in $F(Ar)$, P and p respectively. Distributions were calculated for the Al(4) emission due to its higher intensity, and subsequent higher resolution.



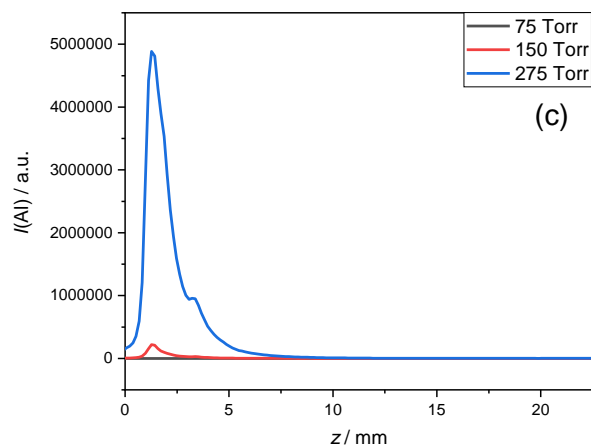


Figure 3.11 – Spatial profiles calculated for a) Al(4) as a function of $F(\text{Ar})$ at base $F(\text{H}_2)$, p and P , b) Al(4) as a function of P at base $F(\text{H}_2)$ and p , and c) Al(4) as a function of p at base $F(\text{H}_2)$ and P , for an Al_2O_3 substrate on a W substrate with $d_{\text{sub}} = 32$ mm and $d_{\text{wire}} = 0.002$ ".

The Al(4) emissions appear to demonstrate a similar profile as in figure 3.9, with $I(\text{Al})$ peaking at approximately 2 mm from the substrate and falling to zero shortly after 5 mm. In figure 3.11a $I(\text{Al})$ exhibits a significant decrease upon the introduction of Ar, falling further still with increasing $F(\text{Ar})$. Figure 3.11b shows a substantial variation in $I(\text{Al})$ with P as with H_β , however at low P , $I(\text{Al})$ is not detected above the background noise. Similarly in figure 3.11c, $I(\text{Al})$ is not visible at low p , but appears to increase with increasing p . In general it can be suggested that as the parameters are increased, so too does T_{sub} and consequently Al will be etched into the plasma as sufficient process conditions. The exception is $I(\text{Al})$ as a function of $F(\text{Ar})$, where the dependency of T_{sub} on $F(\text{Ar})$ working to increase $[\text{Al}]$ is suggested to be outweighed by Ar acting as a quencher of the investigated excited state of Al. The quenching mechanism of excited state Al in this plasma is currently unknown, and may likely involve H, H_2 and Al species, however upon the introduction of the heavier Ar species it is likely further quenching will occur. For both P and p , Al demonstrates an increased emission intensity when increasing the parameter, and this can be attributed to the rising T_{sub} . For this reason, $I(\text{Al})$ is not seen at low P and p , as T_{sub} is not sufficient to etch Al into the gas phase. The Al_2O_3 T_{sub} can be assumed to be the variable source of Al in the gas phase, from the plume emissions seen in figure 2.2. The variation with both P and p are not linear, inferring that these emissions are also affected by additional plasma parameters.

The behaviour of Al emission in regards to plasma conditions is interesting, however the introduction of Al to the gas phase was primarily to probe the thermal component of the EEDF. OES has been used to estimate T_e from emission intensities from two differing energy levels of a species in its excited states, for example the intensity ratio of H_α and H_β emissions.⁶ The $n = 3$ and $n = 4$ energy levels are populated by direct EI, and therefore the ratio of line intensities are proportional to the ratio of rate constants for EIE, and T_e can then be calculated through a stationary Boltzmann equation. For Al it has been discussed that the Al(1) and Al(2), and Al(3) and Al(4) appear to vary in doublets respectively and that a ratio between the Al(1) and Al(4) would be most relevant. The ratio of two emitting states can be related to one another as illustrated in equation 9.¹² The ratio of $k_Q[\text{Al}]$ is assumed to be one, with both states quenching at the same rate and the detection efficiency ratio for Al(1) and Al(4) has been estimated as approximately 3.5 from previous data. The ratio of $\eta(E)$ can then be related to $k_B T_e$ through the Boltzmann distribution described in equation 11. Neglecting accurate values of $k_Q[\text{Al}]$ and ε , and degeneracies this can be rearranged to form equation 12:

$$k_B T_e = \frac{\ln\left(\frac{I(\text{Al}(1))\lambda_{\text{Al}(1)}A_{\text{Al}(1)}}{I(\text{Al}(x))\lambda_{\text{Al}(x)}A_{\text{Al}(x)}}\right)}{\Delta E} \quad (12)$$

where x is the Al emission line being compared to Al(1). Ma *et al.* suggest an expected $k_B T_e$ of approximately 1.3 eV, and using the values for Al(1) and Al(4) in equation 12, an emission ratio of approximately 1.27 is calculated.¹² The ratio of $I(\text{Al}(4))$ and $I(\text{Al}(1))$ may be calculated from experimental data across the full height of the plasma, however as previous figures demonstrate $I(\text{Al})$ is limited to a typical z range of 0 to 5 mm, peaking at approximately 2 mm. It is therefore reasonable to estimate $k_B T_e$ using the maximum $I(\text{Al})$ for each emission. For Al(4) and Al(1) at base conditions this would yield an emission intensity ratio of approximately 12.9, an order of magnitude higher than the value calculated from a known $k_B T_e$. Using the measured emission intensity ratio, a $k_B T_e$ of approximately 0.29 eV is calculated, a significant underestimate. It is likely that $k_Q[\text{Al}]$ and ε are responsible to some extent for this underestimate, however altering these to physically realistic values would decrease the estimate further.

A Boltzmann plot offers an alternative method for estimating $k_B T_e$, through using a range of Al emissions in equation 12. There are a number of Al I emissions detected near 257 nm and 266 nm that offer emission intensity ratios to Al(1), in order to form the Boltzmann plot using the values in figure 3.8a, as presented in figure 3.12.

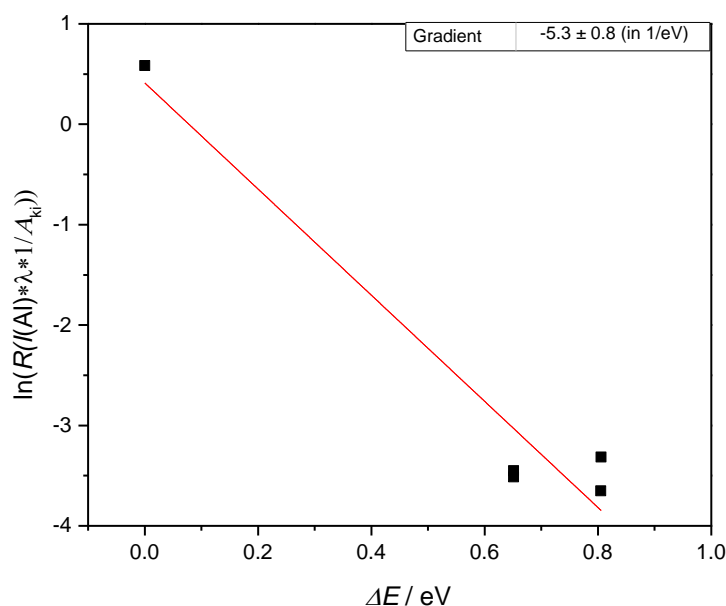


Figure 3.12 – Boltzmann plot of emission intensity ratios between Al(1) and Al emissions at 256.9 nm, 257.7nm, 265.5 nm, 266.2 nm and Al(2).

The horizontal axis is defined as the energy difference between the upper states of Al (1) and the emissions plotted, and the vertical axis is the natural log of the $I(\text{Al})$, λ and A_{ki} ratios, denoted as R . The data points represent ratios between Al(1) and emissions at 256.9 nm, 257.7 nm, 285.5 nm, 266.2 nm and Al(1). It is noted that due to the high intensity of Al(1) and Al(2), relative to the other emissions the linear relationship is mainly captured by the Al(1) and Al(2) ratio. The gradient of this Boltzmann plot is equal to the negative reciprocal of $k_B T_e$, giving a value for $k_B T_e$ of approximately 0.19 ± 0.02 eV, a similar underestimate as the previous method.

There are a number of reasons why Al resulted in an underestimate of $k_B T_e$. Firstly for the emission intensity ratio of Al(1) and Al(4), the estimated value for the ratio of ε and $k[Q]$ may not be accurate. It is likely that ε is at least of the correct magnitude, and does not account for the magnitude underestimate in $k_B T_e$. An uncertainty in $k[Q]$ however, will arise if the two states undergo different quenching processes, and as noted the quenching process of Al excited states are unknown. The order of magnitude underestimate in Al(4):Al(1) may indicate a quenching process involving two different quenchers, H₂ and H, which exist at [H₂]:[H] of approximately 10 to 1. The underestimate in the Boltzmann plot is likely due to the linear relationship being falsely projected by the emission intensity ratio of Al(1) and Al(2), and in fact the intensity ratios of multiple Al emissions do not form a linear relationship against the difference in the upper energy states. This could be checked by comparing more emissions, however the OES λ range is not large enough to capture more emissions in the same detection.

3.4 Cavity Ring Down Spectroscopy of Silicon Atoms

CRDS was used to investigate ground state Si atoms in the gas phase, introduced through an additional flow of SiH₄. This was carried out under varying process conditions, and column density measurements were achieved for Si, denoted as {Si}, as a function of z , $X_0(\text{SiH}_4)$, p , P and $F(\text{CH}_4)$. In section 2.1.3 and 2.3 the specific flow rates for CRDS experiments were discussed, and the specific base conditions were defined at $P = 1.5$ kW, $p = 150$ Torr, $F(\text{SiH}_4) = 0.5$ sccm and $F(\text{H}_2)_{\text{total}} = 600$ sccm, where $F(\text{H}_2)_{\text{total}} = F(\text{H}_2)_{\text{cavity}} + F(\text{H}_2)_{\text{arms}}$, and $F(\text{H}_2)_{\text{cavity}} = 300$ sccm and $F(\text{H}_2)_{\text{arms}} = 300$ sccm. $F(\text{H}_2)_{\text{cavity}}$ and $F(\text{H}_2)_{\text{arms}}$ were kept equal when varying $F(\text{H}_2)_{\text{total}}$. A baseline ring-down lifetime (τ) was defined with a H plasma present, and upon the introduction of SiH₄ the λ was driven and absorption monitored through the method described in section 2.3.

Before carrying out CRDS absorption measurements, the setup required daily optimisation to ensure a level of reproducibility to the column densities. In order to achieve a baseline τ of more than 200 ns and maintain a relatively low MSE, both variables were monitored through the LABVIEW programs. A number of nuances to the CRDS set up lead to a gentle rise in MSE during experimentation, and large MSE values at high values of $\Delta\tau$ and z , where {Si} is increasing. The doubling crystal used in the beam optics between the dye laser and the periscope would shift its alignment over the experimental day, due to energy transfer from the high power laser leading to thermal vibration within the crystal. It was also necessary to ensure the laser path was level through the cavity and reflecting perpendicularly off both mirrors, so that light transmitted through the exit mirror was suitably collected in the photomultiplier tube that the τ signal exhibited the characteristic exponential decay. τ varied with the absorbance of Si for the three $\lambda = 251.432$ nm ($J = 0$), 252.411 nm ($J = 1$) and 252.851 nm ($J = 2$), alongside a continuous sinusoidal etalon transmission scan, as introduced in section 2.2.2.⁷ The etalon trace varied independent of absorbance, and used as a means to calibrate the $\bar{\nu}$. It was then important to capture the range of two etalon peaks when detecting changes in τ , so that the $\bar{\nu}$ width of the absorption peak could be calibrated against the etalon trace and subsequently $\bar{\nu}$, as illustrated for $J = 1$ in figure 3.13. This also ensured the λ grating was driven at a constant speed, as slower driving speeds would lead peak broadening and overestimates in area.

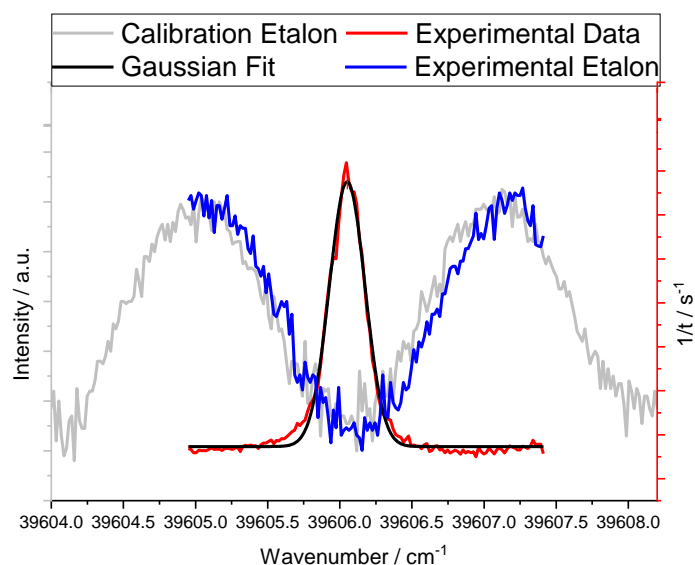


Figure 3.13 – An example of Si absorption peak calibration with a Gaussian fit and etalon traces for $J = 1$ at base conditions: $P = 1.5$ kW, $p = 150$ Torr, $F(\text{SiH}_4) = 0.5$ sccm and $F(\text{H}_2)_{\text{total}} = 600$ sccm.

3.4.1 H/Si Plasma

Initially a distribution of $\{\text{Si}\}$ across the full height of the base plasma was defined at base conditions, as shown in figure 3.14, by varying z as described in section 2.3 through replacing the side viewports with arms attached by flexible bellows to the variable platform. These side arms formed the linear cavity, and along with the mirrors were adjustable to the full height of the plasma. The z values are taken from a $z = 0$ marking the height at which the substrate obstructs transmission of the laser, thus suppressing the characteristic exponential decay.

Under base conditions in a H/Si plasma, $\{\text{Si}\}$ is seen to rise steadily with height above the substrate. The MSE represented in the error bars are also shown to increase with z , due to larger $\{\text{Si}\}$ as noted previously. It may be suggested the gentle rise in $\{\text{Si}\}$ with z can be explained by Si thermodiffusing in the plasma; present in its lowest densities in the hotter regions closer to the substrate and at its highest density in the cooler regions near the periphery of plasma. It is also possible that the base plate may act as a sink of Si species, due to the typical adsorption of species to the surface, or upon the addition of CH_4 , the known incorporation of Si into a CVD diamond surface.

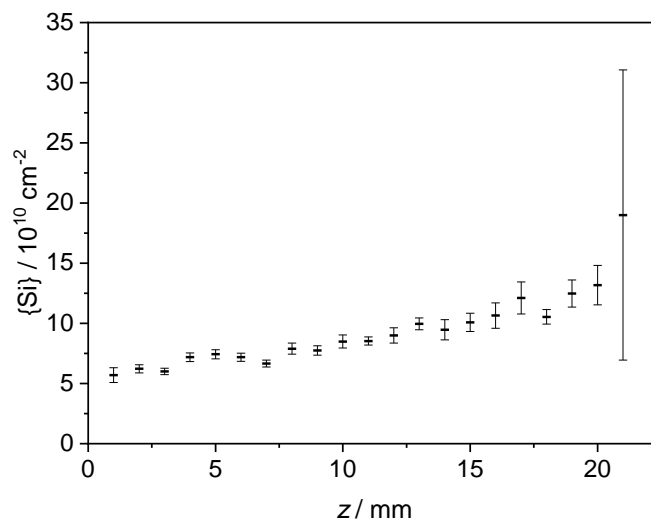


Figure 3.14 - $\{\text{Si}\}$ for $J = 1$, as a function of z for a H/Si plasma at base conditions.

After assessing the spatial distribution of Si under base conditions, three heights; 5.0 mm, 11.0 mm and 18.3 mm were selected as local maxima in τ to achieve the best resolution and to cover the range of heights of the plasma. $\{Si\}$ was then investigated as a function of $F(SiH_4)$, p , and P for H/Si plasma. In a similar manner to $\{Si\}$ as a function of z , $\{Si\}$ was expected to show a similarly linear increase with increasing $F(SiH_4)$. Initial assessments for $\{Si\}$ as a function of $F(SiH_4)$, presented at a molar fraction, $X_0(SiH_4)$ were undertaken for absorption transitions for $J = 1$ and $J = 2$, as shown in figure 3.15a.

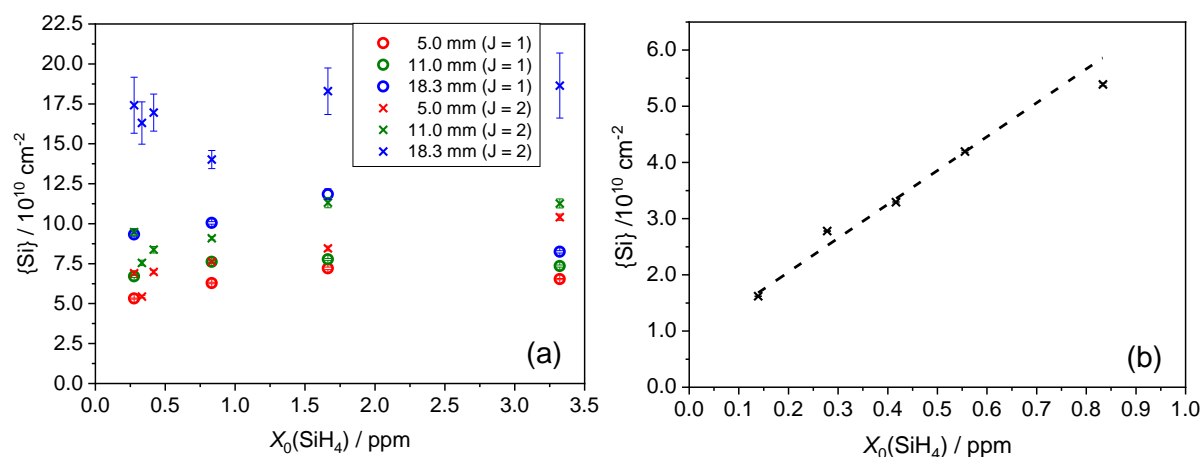


Figure 3.15 – a) $\{Si\}$ for $J = 1$ and $J = 2$, at 3 values of z , as a function of $X_0(SiH_4)$ for a H/Si plasma, and b) $\{Si\}$ for $J = 0$, as a function of $X_0(SiH_4)$ for a H/Si plasma, corrected for $\Delta X_0(\text{gas})$.

Figure 3.15a appears to confirm the observations from figure 3.14, with $\{Si\}$ increasing with the three heights consistently for each value of $X_0(SiH_4)$. The relationship of $\{Si\}$ with $F(SiH_4)$ however, is not distinctly demonstrated, and for $X_0(SiH_4) = 3.3 \text{ ppm}$, $\{Si\}$ shows a decrease for the values of z and J . It is noted that, as mentioned in section 2.1.3 $F(SiH_4)$ was not varied independently due to the relative sensitivity of $F(SiH_4)$, but instead through varying $F(H_2)_{\text{total}}$, an effective variation in $X_0(SiH_4)$ was achieved. Subsequently relatively small changes in $F(H_2)$ may result in large variation in $X_0(SiH_4)$, and it was reasoned that the rate of gas removal from the deposition chamber, either through the gas exhaust or chamber leak would negatively impact $X_0(SiH_4)$ due to $\Delta X_0(\text{gas})$, affecting $\{Si\}$. $\{Si\}$ as a function of $X_0(SiH_4)$ was then repeated with $J = 0$, however correcting for $\Delta X_0(\text{gas})$ by varying $F(SiH_4)$ and maintaining a large constant $F(H_2)_{\text{total}} = 1800 \text{ sccm}$, where $\Delta X_0(\text{gas})$ was proportional to the reciprocal of $F(H_2)$ and the result is presented in figure 3.15b. $\Delta X_0(\text{gas})$ suggests that Si was involved with reactions with additional species such as H_2O , limiting the response of $\{Si\} X_0(SiH_4)$. Figure 3.15b exhibits a clear positive increase of $\{Si\}$ with increasing $X_0(SiH_4)$, suggesting a linear trend. It is important to note that $J = 0$, $J = 1$ and $J = 2$ are expected to fundamentally vary the same with conditions. After investigating $\{Si\}$ with $F(SiH_4)$, $\{Si\}$ was then probed as a function p between 50 and 250 Torr, and as a function of P between 0.70 kW and 1.85 kW. This is presented in figures 3.16.

Figure 3.16a illustrates the behaviour of $\{Si\}$ for $J=1$ and $J=2$, at the three different values of z and excluding a margin of variation at 250 Torr for some values of z and J , $\{Si\}$ unmistakably increases with raising p . Figure 3.16b appears to show the opposite trend, decreasing in $\{Si\}$ with increasing P . The tendency of $\{Si\}$ to increase with p suggests Si behaving somewhat ideally, increasing in abundance as p increases. Although $\{Si\}$ does appear to decrease with P , this is hard to explain as P has a complex effect on gas phase chemistry. One suggestion is as the plasma expands with increasing P , the radial cooler regions shrink, thus $\{Si\}$ decreases.

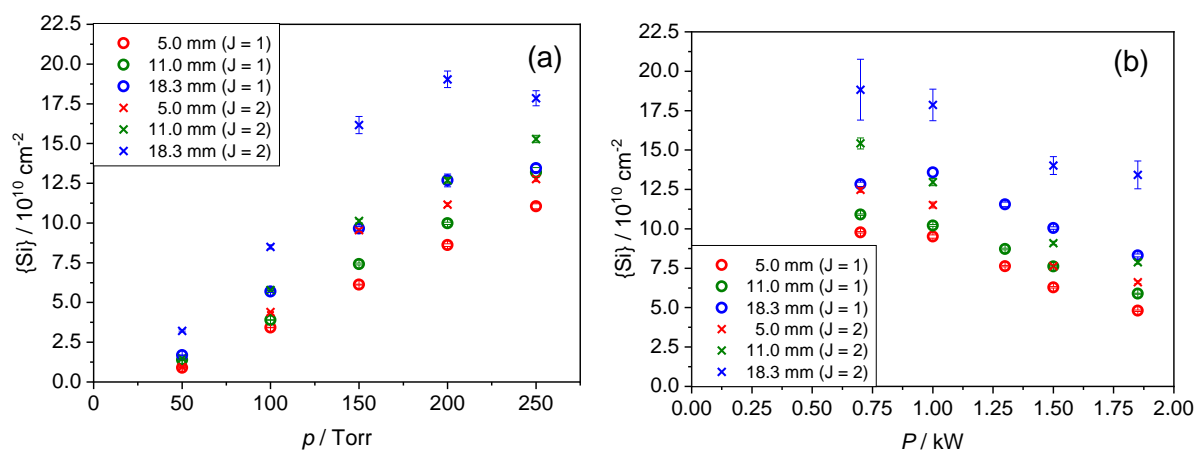


Figure 3.16 – a) $\{Si\}$ for $J = 1$ and $J = 2$, at 3 values of z , as a function of p for a H/Si plasma and b) $\{Si\}$ for $J = 1$ and $J = 2$, at 3 values of z , as a function of P for a H/Si plasma.

3.4.2 H/C/Si Plasma

CRDS measurements of $\{Si\}$ were carried out for H/C/Si plasmas using the $J = 2$ absorption transition. Initial observations suggested a decrease in Si upon the introduction of CH_4 to the input gas. $F(H_2)$ was compensatory lowered to maintain a constant $X_0(CH_4)$ when varying $X_0(SiH_4)$, and a constant $X_0(SiH_4)$ when varying $X_0(CH_4)$. Figures 3.17 present $\{Si\}$ as a function of $X_0(SiH_4)$ and $X_0(CH_4)$.

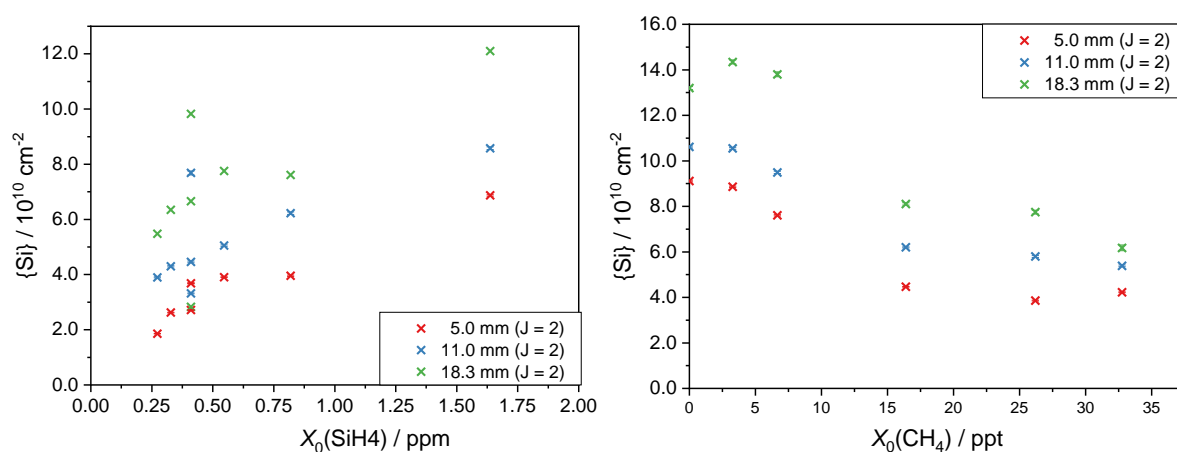


Figure 3.17 – a) $\{Si\}$ for $J = 2$, at 3 values of z , as a function of $X_0(SiH_4)$ for a H/Si plasma and b) $\{Si\}$ for $J = 2$, at 3 values of z , as a function of $X_0(CH_4)$ for a H/Si plasma.

As in the solely H/Si plasma, $\{Si\}$ still increases with SiH_4 with CH_4 present as illustrated in figure 3.17a, more linearly at low z . The figure supports the positive relationship between $\{Si\}$ and $X_0(SiH_4)$, and theoretically $F(SiH_4)$ for a constant $X_0(CH_4)$. As noted $\{Si\}$ appears to decrease in the presence of CH_4 and with increasing $X_0(CH_4)$, as displayed in figure 3.17b. The fall in $\{Si\}$ is more significant at lower $X_0(CH_4)$, and at the three highest $X_0(CH_4)$ the change is relatively minimal. It can be said that when increasing $X_0(CH_4)$, $\{Si\}$ decreases up to $X_0(CH_4)$, and then remains relatively constant. This might be attributed to $[Si]$ reacting with CH_x species preferentially over $[C_2H_2]$ to form of SiC species. $X_0(CH_4)$ varies a number of magnitudes more than $X_0(SiH_4)$, but through varying $F(H_2)$ the fall in $\{Si\}$ with $X_0(CH_4)$ is not due to an increase in CH_4 content. Above approximately 20 ppt $X_0(CH_4)$, C_2H_2 becomes the dominant species as discussed in section 1.3.1. It is deduced that Si atoms react preferentially with CH_x ($0 \leq x \leq 4$) species when compared to C_2H_2 , accounting for the relatively constant $\{Si\}$ at $X_0(CH_4) > 20$ ppt.

As with H/Si plasmas, {Si} was also investigated as a function p between 50 and 250 Torr, and as a function of P between 0.70 kW and 1.85 kW as shown in figures 3.18.

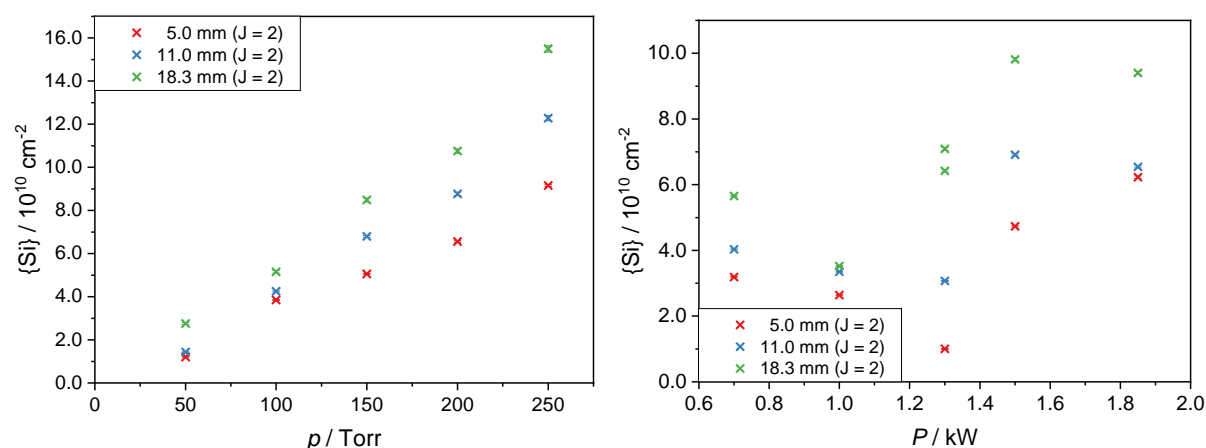


Figure 3.18 – a) {Si} for $J = 2$, at 3 values of z , as a function of p for a H/Si plasma and b) {Si} for $J = 2$, at 3 values of z , as a function of P for a H/Si plasma.

Figure 3.18a shows that in the H/C/Si plasma, {Si} appears to vary with p as in a H/Si plasma, with {Si} increasing linearly with increasing p . In figure 3.18b, the behaviour of {Si} with P in the presence of CH_4 appears very uncertain, supposedly falling from low P to medium P , and rising again at higher P for $z = 5.0$ mm and 11.0 mm. This suggests a complex chemistry between Si and C with varying P . Besides P , the behaviour of {Si} in H/C/Si plasmas appear comparably similar to that of H/Si plasmas. With no practical limitations, it would have been beneficial to carry out a number of CRDS experiments again in order to further gauge or confirm the relationships seen in this discussion.

3.5 References

- 1 E. J. D. Mahoney, S. Mushtaq, M. N. R. Ashfold and Y. A. Mankelevich, *J. Phys. Chem. A*, 2019, **123**, 2544-2558
- 2 E. J. D. Mahoney, B. S. Truscott, S. Mushtaq, M.N.R. Ashfold and Y. A. Mankelevich, *J. Phys. Chem. A*, 2018, **122**, 8286-8300
- 3 M. N. R. Ashfold, E. J. D. Mahoney, S. Mushtaq, B. S. Truscott and Y. A. Mankelevich, *Chem. Commun.*, 2017, **53**, 10482-10495
- 4 I. Banerjee, N. V. Kulkarni, S. Karmaker, V. L. Mathe, S. V. Bhoraskar and A. K. Das, *Plasma Sci. Technol.*, 2010, **12**, 27-30
- 5 P. Sankar, J. J. J. Nivas, N. Smijesh, G. K. Tiwari and R. Philip, *J. Anal. At. Spectrom.*, 2017, **32**, 1177-1185
- 6 N. Derkaoui, C. Rond, T. Gries, G. Henrion and A. Gicquel, *J. Phys. D: Appl. Phys.*, 2014, **47**, 205201-205210
- 7 NIST Atomic Spectra Database, https://physics.nist.gov/PhysRefData/ASD/lines_form.html, (accessed April 2019)
- 8 F. O. Jones and K. O. Wood, *Br. J. Appl. Phys.*, 1964, **15**, 185-187
- 9 X. Yang and P. J. Dagdigian, *J. Chem. Phys.*, 1998, **109**, 8920-8928
- 10 P. Patnaik, *Handbook of Inorganic Chemicals*, McGraw-Hill, New York, 2003
- 11 **CC** – E. J. D. Mahoney, B. S. Truscott, M. N. R. Ashfold and Y. Mankelevich, *J. Phys. Chem. A*, 2017, **121**, 2760-2772
- 12 J. Ma, J. C. Richley, M. N. R. Ashfold and Y. A. Mankelevich, *J. Appl. Phys.*, 2008, **104**, 103305-103309

4. Conclusions and Further Work

Two spectroscopic methods; OES and CRDS were used to investigate a number of gas phase species of H based MW activated plasmas, and the results discussed in the previous section lead to several propositions regarding the specific gas phase species.

4.1 Substrate Temperature Control

The initial investigation in this thesis involved the use of OES to determine changes in MW activated H based plasmas when varying parameters that impact the t_{sub} . The first OES measurements probed the H_α and $H_2(d-a)$ transitions, which are sensitive to the hyperthermal component of the EEDF, with $I(H_\alpha)$ and $I(H_2(d-a))$ generally maximising at low z , approximately 2 mm above the substrate, under enhanced conditions. The centre of the plasma appeared less affected by changes in substrate, only through variations in the overall emission intensity. The H_α and $H_2(d-a)$ emissions were investigated as a function of varying d_{sub} , d_{wire} , and $X_0(Ar)$, to establish the variation of the hyperthermal component of the EEDF and a crude t_{sub} control.

Increasing $X_0(Ar)$, decreasing d_{sub} and increasing d_{wire} all acted independently to raise t_{sub} . Increasing d_{sub} and d_{wire} raised the absolute intensities of both H_α and $H_2(d-a)$ emissions at low z , by enhancing the hyperthermal component of the EEDF. It was suggested from investigating the latter parameter, that H_α was more sensitive than $H_2(d-a)$ to the experimental variation arising from opening and closing the deposition chamber between measurements. Introducing Ar reduced both $I(H_\alpha)$ and $I(H_2(d-a))$ overall, but enhanced the relative intensities at low z , which previous literature has attributed to near resonant energy transfers between excited states of Ar, H and H_2 .¹ Although most of these parameters have already been explored, the variation of d_{wire} with $d_{sub} = 17$ mm is unique, and highlighted that the hyperthermal component of the EEDF close to the substrate can be substantially manipulated.

The investigation into the effect of substrate conditions carried out in this study was informative, but by no means comprehensive. Although a number of means of impacting T_{sub} was investigated, each variable was not exhaustively explored and in order to form a better picture of these behaviours, emissions under more condition values and over an expanded condition range would need to be measured. Continued experimentation into these parameters would affirm their relationship to T_{sub} , but the use of a single spectroscopic technique, although practical limits the efficacy of such an investigation.

4.2 Probing Electron Energy Distribution Functions through Aluminium Emissions

The secondary use of OES involved the introduction of Al into the gas phase in an attempt to probe the thermal component of the EEDFs, currently inaccessible through OES measurements, and subsequently develop a tool to estimate $k_B T_e$. Al was integrated into the gas phase of H based plasmas through the successful surface etching of an Al_2O_3 substrate, and Al emissions were detected over several λ ranges. Under base conditions, $I(Al)$ can be observed through a number of emissions, most prominently the Al I lines seen at 308.22 nm and 309.27 nm due to $3s^23d \rightarrow 3s^23p$, and 394.40 nm and 396.15 nm due to $3s^24s \rightarrow 3s^23p$, referred to as Al (1), Al(2), Al(3) and Al(4) respectively.

The ratio within these two pairs of doublets demonstrated near 2:1 ratios to one another, and these ratios were seen to persist experimentally. As the two pairs of emissions originate from common upper states, the ratios can be explained in terms of their relative g_i and respective A_{ki} . $k_B T_e$ was estimated using a Boltzmann relationship, by comparing the ratio of intensities

of one emission from each pair. Under such a calculation, $k_B T_e$ was underestimated by an order of magnitude. This may perhaps be indicating the need for different $k_Q[\text{Al}]$, and a sensible estimate may yet be achievable with an accurate estimation of the quenching process of the two excited Al states through a 2D kinetic study. Alternatively, it may be inferring a quenching process with $[\text{H}]$ and $[\text{H}_2]$, which hold a similar ratio, as the quenchers for the Al(4) and Al(1) state respectively. Further attempts to estimate $k_B T_e$ were carried out through the use of a Boltzmann plot and a range of additional Al emissions, however these also under predicted $k_B T_e$. Further work would be to test the same emissions against the other pair of emitting Al lines. If all of these states were indeed quenched by different species, this could yet yield an T_e .

Al does not appear to function as a probe of the thermal component of the EEDF. The Al substrate did not allow for a stable plasma, and the Al_2O_3 substrate did not yield a sensible T_e . At least at first assessment, Al does not offer a solution to the challenge of effectively measuring the T_e of MW plasmas. Al_2O_3 did offer an insight into the impact of a ceramic substrate on the plasma, suggesting a potentially higher power absorption and further links to T_{sub} control. One flaw of this study was the localisation of $I(\text{Al})$ to $z < 6$ mm, limiting the EEDF probe ambition. Further still, the emission above the Al_2O_3 substrate appears as a plume, suggesting that despite attempts to influence T_{sub} , Al was not controllably introduced into the gas phase. Several means to improve and expand upon such a study would be to find a means to introduce diluted Al into the gas phase through a gaseous form or volatile liquid such as Al tributyl. Alternatively pre-vaporisation of Al powder could encourage an even distribution of Al in the gas phase or the introduction of another emitting species with a range of emitting thermal states, for instance $I(\text{Si})$ through SiH_4 . Another semi-volatile metal or ceramic substrate, with visible emissions may also offer a probe of T_e . If continued work was carried out with Al and Al_2O_3 , it could prove interesting to investigate the impact of ceramic substrates on the plasma, or as a comparison with other metallic and ceramic substrates. Likewise, the continued investigation into Al could warrant the weighing of substrates before and after experimentation, due to the visible deposition or tarnishing of both Al and Al_2O_3 surfaces.

As with investigations into T_{sub} , the impact of a range of parameters was examined through monitoring the variation of $I(\text{H}_\beta)$ and $I(\text{Al})$ as a function of conditions. In addition to the variation of $F(\text{Ar})$, and to a degree d_{wire} , p and P were explored. It is noteworthy that the energy of the upper states of Al^* are significantly less than H^* , thus the presence of a substrate itself is likely enhancing the low z $I(\text{Al})$ contribution. In a similar manner Al emissions were localised to low z , highlighting a symptom of the introduction method. $I(\text{Al})$ was not visible at low p and P , however demonstrated increased emission intensities with increasing p and P , attributed to a higher T_{sub} . Upon increasing these parameters, there is an associated increase in the T_{sub} of Al_2O_3 , and it is suggested that once a threshold temperature is crossed, the introduction of Al into the gas phase is facilitated. The variation with both p and P are not linear, inferring that these emissions are also impacted by additional plasma parameters. There may also be a time dependence on Al emissions, as the Al_2O_3 surface gradually erodes, the composition of the substrate will vary. Such a parameter has not been accounted for and could make an interesting further study.

$I(\text{Al})$ exhibited a decrease with Ar addition, and considering the dependency of T_{sub} on $F(\text{Ar})$, the decrease in $I(\text{Al})$ with increasing $X_0(\text{Ar})$ is an unexpected result. The ensuing inference is that Ar is a quencher of the investigated excited state of Al. The H Balmer emissions examined in the presence of an Al_2O_3 substrate demonstrate notably different trends to those in the T_{sub} study. This indicates significant changes to the hyperthermal component of the EEDF when

Al is present. The spatial distributions of the H emissions captured by these ranges were calculated, and exhibited an enhancement of $I(H_\beta)$, $I(H_\lambda)$ and $I(H_\delta)$ at low z with an Al_2O_3 substrate present. On comparison of $I(H)$ between studies with and without an Al_2O_3 substrate, there is a notable difference in spatial distributions and trends with varying process conditions. It seems probable that the changes in spatial distribution are to some extent attributed to substantial local changes in the I^E/N from the presence of an additional, smaller substrate. This is reinforced by similar observations when using a smaller d_{sub} . The suggestion is that the presence of smaller objects increase the I^E/N . An interesting follow on study, more relevant to the CVD of diamond, would be to investigate how these emission intensities vary upon the addition of Si and diamond substrates of varying d_{sub} .

The different trends seen with common parameters, between the investigation into T_{sub} and Al can be understood from variations in the hyperthermal component of the EEDF. This was evident in both $I(H_\alpha)$ and $I(H_2(d-a))$, which maximised at low z , approximately 2 mm above the substrate of $d_{sub} = 17$ mm. $I(H_\alpha)$ and $I(H_2(d-a))$ plainly demonstrated an enhancement at such heights with increasing d_{wire} when using this d_{sub} , while the plasma core appears less affected. Without an additional Al_2O_3 substrate there is an observed enhancement of the I^E/N , and consequently the hyperthermal component of the EEDF, evidenced by this increased $I(H)$ at low z . Whereas increasing d_{wire} with an Al_2O_3 substrate present acted to decrease low z $I(H)$. This can be attributed to an increase in the T_{sub} , encouraging the generation of gas phase [Al]. Al has a significantly lower ionization energy when compared to H or H_2 , thus would act to increase thermal η_e and decrease the hyperthermal component. Consequently, increasing d_{wire} reduces $I(H)$. The shift in the prominent cation can also explain the more subtle behaviours of $I(H)$ with parameters such as p and P , such as the transition from no $I(Al)$ to large $I(Al)$ upon raising p and P to base conditions. To distinguish which of these effects can be attributed to the presence of a substrate and Al being present in the gas phase, additional materials should be explored as future work.

4.3 Cavity Ring Down Spectroscopy of Silicon Atoms

The use of CRDS in this project was to investigate the introduction of Si into the gas phase, through the addition of SiH_4 under varying plasma conditions. The nature of Si in the CVD of diamond, as both an impurity and a SiV centre, suggests an improved understanding of H/Si and H/C/Si plasmas would be beneficial. $\{Si\}$ was measured as a function of z , $X_0(SiH_4)$, p , P and $X_0(CH_4)$ in MW activated H/Si and H/C/Si plasmas, offering an insight into the distribution of ground state Si, and once combined with 2D modelling and further H/C/Si studies will help further the understanding of the prominent gas phase chemistries of these two systems. Initially $\{Si\}$ was measured as a function of z , suggesting an increasing $[Si]$ at higher and cooler z , and supposedly also higher r assuming a degree of 2D symmetry to the gas phase. Such measurements are therefore not probing the hot plasma regions. It was deduced that $[Si]$ maximises at lower T_{gas} and may be assumed to thermodiffuse to the plasma periphery. Si was deduced to have a complex behaviour with varying $X_0(SiH_4)$ in a simple MW activated H/Si plasma. The discrepancy between altering $X_0(SiH_4)$ through variation in $F(SiH_4)$ and $F(H_2)$ was reconciled by the consideration of an $F(H_2)$ dependent air leak, and that $\{Si\}$ was sensitive to such a leak. Generally $\{Si\}$ increased proportionally with increasing $X_0(SiH_4)$ and as a function of p , when both effective H_2 and H_2/CH_4 fractions remained constant. The behaviour of $\{Si\}$ as a function of P was similarly explored, but offered a difficult interpretation without additional computational modelling. Upon the addition of methane, $X_0(CH_4)$, many of these results were reproduced. When increasing $X_0(CH_4)$, $\{Si\}$ decreases up to $X_0(CH_4)$, and then

remains relatively constant. This might be attributed to [Si] reacting with CH_x species preferentially over $[\text{C}_2\text{H}_2]$. Further work of relevance to diamond CVD, and particularly of interest to using Si substrates, might be to compare spatially resolved spatial distributions of the Si ground state to those achieved when a Si substrate is present. Upon the introduction of CH_4 , it is deduced that Si atoms react preferentially with CH_x ($0 \leq x \leq 4$) species, when compared to C_2H_2 .

It is unfortunate that the air leak attributed to the CRDS mirrors is significantly larger than the investigated $X_0(\text{SiH}_4)$, 10 ppm as opposed to 0.83 ppm under base conditions. Future work may be to investigate the $\text{Si}(^1\text{D}_2)$ state with CRDS. Such a state will have a significantly lower [Si], facilitating a higher $X_0(\text{SiH}_4)$ to be investigated, and would enable absorption access to the hotter plasma regions, whereby $\text{Si}(^1\text{D}_2)$ might be expected to maintain higher thermal populations. The CRDS of Si was suggested as further work in a previous spectroscopic study into H/Si and H/C/Si plasmas.² This study also suggested further OES investigation into Si containing plasmas, specifically H/C/Si plasmas in an effort to observe small Si and C containing species and investigated SiH in the gas phase through OES, and subsequently a CRDS study of SiH may prove supplementary. Due to the limitations of this study, the CRDS investigation into Si would also benefit from additional experimentation and computational modelling of H/Si and H/C/Si plasmas. Finally, with substrate variation acting as a linking focus in this study, alongside additional work into substrate conditions and materials, and investigation into controllable substrate etching in MWPCVD could prove beneficial to future work.

4.4 References

1. E. J. D. Mahoney, S. Mushtaq, M. N. R. Ashfold and Y. A. Mankelevich, *J. Phys. Chem. A*, 2019, **123**, 2544-2558
2. A. Lalji, Masters Thesis, University of Bristol, 2018